Inferring global terrestrial carbon fluxes from the synergy of Sentinel 3 & 5P with Gaussian process hybrid models

Pablo Reyes-Muñoz [a,*], Dávid D.Kovács [a], Katja Berger [a,b], Luca Pipia [c], Santiago Belda [d], Juan Pablo Rivera-Caicedo [e], Jochem Verrelst [a]

[a] IPL - Image Processing Laboratory, University of Valencia, Catedrático Agustín Escardino Benlloch 9, Paterna, 46980, Spain
[b] GFZ German Research Centre for Geosciences, Telegrafenberg, 14473, Postdam, Germany
[c] ICGC - Institut Cartogràfic i Geològic de Catalunya, Parc Montjuïc s/n, Barcelona, 08038, Spain
[d] University of Alicante, Applied Mathematics, Space Geodesy Group, Parc Montjuïc s/n, Alicante, 03690, Spain
[e] Secretary of Research and Graduate Studies, CONACYT-UAN, Tepic 63155, Mexico

ARTICLE INFO

ABSTRACT

The ongoing monitoring of terrestrial carbon fluxes (TCF) goes hand in hand with progress in technical capacities, such as the next-generation Earth observation missions of the Copernicus initiative and advanced machine learning algorithms. Proceeding along this line, we present a physically-based data-driven workflow for quantifying gross primary productivity (GPP) and net primary productivity (NPP) at a global scale from the synergy of Copernicus' Sentinel-3 (S3) Ocean and Land Color Instrument (OLCI) and the TROPOspheric Monitoring Instrument (TROPOMI) onboard Sentinel-5 Precursor (S5P), along with meteorological variables from Copernicus ERA5-Land. Specifically, we created generic hybrid Gaussian process regression (GPR) retrieval models combining S3-OLCI-derived vegetation products with the TROPOMI solar-induced fluorescence (SIF) product to capture global GPP and NPP. First, the GPR algorithms were trained on theoretical simulations through the Soil-Canopy-Observation of Photosynthesis and Energy fluxes (SCOPE) model, with the final retrieval models termed SCOPE-GPR-TCF. Second, the SCOPE-GPR-TCF models were integrated in Google Earth Engine (GEE) and fed with satellite data and products (coming from Sentinel 3 & 5P and ERA5-Land), producing global and regional (Iberian Peninsula) maps at spatial resolutions of 5 km and 300 m during the year 2019. Moderate relative uncertainties in the range between 10%–40% of the GPP and NPP estimates were achieved by the SCOPE-GPR-TCF models. Analysis of the driving variables revealed that the S3-OLCI vegetation products, i.e., leaf area index (LAI), the fraction of absorbed photosynthetically active radiation (FAPAR), and SIF provided the highest prediction strengths. Validation of GPP temporal estimates from GPR against partitioned GPP estimates at 113 flux towers located in America and Europe highlighted a good overall consistency at the local scale, with performances varying depending on the site and vegetation type. The highest scores emerged for stations located in croplands, grasslands, deciduous broad-leaf and evergreen needle-leaf forests with top R^2 and *rmse* values above 0.8 and below 2 μmol m^{-2} s^{-1} respectively. Further, benchmarking spatiotemporal analysis revealed a strong intra-annual global correlation against reference products for the same year 2019: (i) Cross-comparison against LPJ-GUESS resulted in modal values of $R = 0.8$ and *rmse* = 1.93 μmol m^{-2} s^{-1} for GPP. (ii) MOD17A2H GPP and NPP estimations cross-correlated with R modal values of 0.94 and 0.92 and *rmse* of 1.26 and 1.05 μmol m^{-2} s^{-1}, respectively. We conclude that the hybrid models integrated into the GEE cloud-computing platform facilitate streamlining the global mapping of TCF products at efficient processing costs. This is particularly promising in preparation for the upcoming Fluorescence Explorer (FLEX) mission, where the SCOPE-GPR-TCF models are foreseen to be customized to 300 m resolution FLEX SIF data streams for high-resolution global productivity monitoring.

* Corresponding author.
E-mail addresses: pablo.reyes@uv.es (P. Reyes-Muñoz), david.kovacs@uv.es (D. D.Kovács), katja.berger@uv.es (K. Berger), luca.pipia@uv.es (L. Pipia), santiago.belda@uv.es (S. Belda), jprivera@uan.edu.mx (J.P. Rivera-Caicedo).

1. Introduction

Monitoring carbon uptake by vegetation has become more relevant than ever due to the urging need for anticipating and mitigating the effects of global climate change, partially regulated through the terrestrial carbon budget (Keenan and Williams, 2018). For instance, according to Friedlingstein et al. (2022), terrestrial carbon sinks accounted for approximately 32% of the total storage, including the ocean and the atmosphere in the budget for the year 2021. The study of terrestrial carbon fluxes (TCF) becomes also important due to its connection with ecosystem services, food, and energy production (Pei et al., 2022).

The rate of photosynthetic carbon assimilated by vegetation is known as gross primary productivity (GPP) (Williams et al., 1997; Beer et al., 2010; Keenan and Williams, 2018; Liao et al., 2023). By additionally accounting for the cellular respiration of vegetation, the net production of biomass can also be quantified. Thus, the net primary productivity (NPP) refers to quantities of carbon stored by vegetation, commonly expressed on a yearly basis (Ruimy et al., 1994). NPP can also be studied over short periods, e.g., days or hours, often associated with the term net photosynthesis (Johnson et al., 1996; Running et al., 2015; Hu et al., 2018). Being the focus of this study, in the following, GPP and NPP are grouped as TCF products. Another related metric is the carbon net ecosystem exchange (NEE), which quantifies the total incoming-outgoing balance of carbon between the atmosphere and land surface, including the respiration of heterotrophic organisms (Bracho et al., 2012).

Although most of the light absorbed by leaves in photosynthesis is used for carbon assimilation (photochemical quenching), a small part is dissipated as heat (non-photochemical quenching), and another part is re-emitted as fluorescence, known as solar-induced chlorophyll fluorescence (SIF) (Schlau-Cohen and Berry, 2015; Wohlfahrt et al., 2018). SIF, the radiant flux emitted between 650 and 800 nm, is therefore the most direct measurable reporter of the photosynthetic machinery in plants (Seaton and Walker, 1990; Porcar-Castell et al., 2014; Mohammed et al., 2019). As such, satellite-based SIF recordings have the potential to offer unprecedented insights into the physiological functioning of vegetation, from leaf to ecosystem scales, and to enhance our ability to model and monitor TCF products in a changing climate (Frankenberg et al., 2014; Sun et al., 2017, 2018; Joiner et al., 2018; Porcar-Castell et al., 2021; Han et al., 2022). Nevertheless, some challenges need to be resolved to be able to derive the full SIF signal from space, such as the weakness of the broadband captured signal (about 1%–5% in the near-infrared, NIR), superimposed upon the integral energy reflected by vegetation (Verrelst et al., 2016c; Vicent et al., 2016). Furthermore, a sufficiently high spatial resolution is required to capture the SIF dynamics at the ecosystem scale (Drusch et al., 2017; Gu et al., 2019). In this context, the Fluorescence Explorer (FLEX) was selected as the eighth Earth Explorer mission of the European Space Agency (ESA) (Drusch et al., 2017) and is expected to be launched in 2026. FLEX will be equipped with the high-resolution spectrometer FLORIS to record the full 650–800 nm SIF signal at 300 m spatial resolution with a repeat cycle of 27 days, allowing the capturing of terrestrial photosynthetic activity across the globe. FLEX will orbit in tandem with Copernicus' Sentinel-3 satellite (S3). As such, the tandem FLEX-S3 mission is foreseen to offer unprecedented opportunities to increase our understanding of the fundamentals of terrestrial vegetation, specifically the process of photosynthesis in plants that leads to carbon fixation (Van Wittenberghe et al., 2021). Awaiting the launch of FLEX, current satellite missions equipped with coarse-spatial-resolution spectrometers able to measure atmospheric gas traces have been exploited to derive single-band SIF at specific high-resolution wavelengths, e.g. within solar Fraunhofer lines (Munro et al., 2016; Crisp et al., 2017; Sun et al., 2018; Guanter et al., 2021; Zhao et al., 2022; Yao et al., 2022). Amongst these atmospheric missions providing single-band SIF products, the TROPOspheric Monitoring Instrument (TROPOMI) onboard Sentinel-5 Precursor (S5P), probably offers the best balance of spatial and temporal resolutions, i.e., 7 km along-track and 3.5 km across-track with a daily global coverage (Veefkind et al., 2012).

Despite the increasing usage of those single-band SIF products as a proxy of TCF (Mohammed et al., 2019; Xiao et al., 2021; Doughty et al., 2023), we are only at the dawn of exploiting the full SIF spectrum using satellites in the context of productivity estimation (Porcar-Castell et al., 2014, 2021). At the same time, there has been ample evidence that established networks of towers can be used to a great extent for inferring TCF maps (e.g., Reichstein et al., 2007; Jung et al., 2009). Particularly, at the local scale, flux towers became the benchmark data stream to determine GPP, NEE, and respiration in different ecosystems (e.g., Baldocchi et al., 2001; Balzarolo et al., 2011; Tramontana et al., 2016). Currently, dedicated flux tower networks provide ground data for the carbon research community, such as FLUXNET (Pastorello et al., 2020). Since flux towers have a spatially restricted footprint and only permit local observations, global mapping is limited and upscaling is required (Jung et al., 2020). In addition, the tower measurements can be used for tuning and validating biogeochemical models and remote sensing estimates.

The quantification of TCF products essentially relies on the principle of light use efficiency (LUE) (Monteith, 1972), relating the rate of photosynthesis to the amount of absorbed photosynthetically active radiation (APAR) by vegetation and LUE, as a function of environmental stress. Driven by the LUE principles, satellite TCF mapping approaches can be classified into the following three main methodological categories:

(I) LUE and VI-based models. Most GPP studies rely on applying LUE formulation (Frankenberg et al., 2011; Dong et al., 2015; Pei et al., 2022). For instance, operationally produced LUE-based TCF products include the Moderate Resolution Imaging Spectroradiometer (MODIS) GPP and NPP products (MOD17A2H) (Running et al., 2015) and the Vegetation Photosynthesis Model (VPM) (Zhang et al., 2017).

(II) Process-based models. They incorporate information on the underlying biochemical and physiological processes of plants following the principles described in Farquhar et al. (1980), Sharkey (1985), Haxeltine and Prentice (1996), Caemmerer (2000). These models are more complex and require a set of variables, such as the electron transport rate, the maximum carboxylation capacity (V_{cmax}), or the stomatal conductance, along with soil variables (e.g. humidity) (Tol et al., 2009a; Han et al., 2022). LPJ-GUESS (Lund-Potsdam-Jena General Ecosystem Simulator) (Martín Belda et al., 2022), ORCHIDEE (Organizing Carbon and Hydrology in Dynamic Ecosystems) (Krinner et al., 2005), BESS (Breathing Earth System Simulator) (Ryu et al., 2011) and BEPS (Boreal Ecosystems Productivity Simulator) (Liu et al., 1997) are examples of process-based models which can be driven by satellite data (e.g. MODIS). The key advantage of process-based models is that they explicitly represent the underlying biological and physical processes that control TCF and can therefore serve more diagnostic than statistical approaches for understanding how TCF responds to changes in environmental conditions and management practices. On the downside, these models typically require a substantial amount of input data and variables, some of which may be challenging to acquire or have limited precision even if they are obtainable (Chen et al., 2023). As an appealing alternative, advanced radiative transfer models (RTMs), such as the Soil Canopy Observation, Photochemistry and Energy fluxes (SCOPE) model (Tol et al., 2009b), include the process-based principles to study TCF (Hu et al., 2018). SCOPE is an integrated vegetation RTM that simulates the interaction of solar radiation with plant canopies, providing a detailed representation of radiative transfer leading to flux simulations and satellite signal reproduction. SCOPE describes radiative and non-radiative energy fluxes in the soil–vegetation–atmosphere system. The RTM can also simulate the SIF emitted by plants, as well as calculate TCF outputs (Prikaziuk et al., 2023), emerging as a physically-based alternative optimal for

application with satellite data and relatively simple as opposed to other process-based models.

(III) Data-driven methods. These methods involve statistical or machine learning (ML) algorithms that utilize in-situ measurements or remotely sensed variables, such as VIs or quantitative vegetation properties, e.g., leaf area index (LAI) and the fraction of absorbed photosynthetically active radiation (FAPAR), to estimate TCF (Beer et al., 2010; Jung et al., 2011; Joiner et al., 2018; Liao et al., 2023). Conventional data-driven methods are commonly developed with site-level observations for spatial upscaling or time series reconstruction (Dou and Yang, 2018; Jung et al., 2020; Tramontana et al., 2020; Balde et al., 2023). When ML models are tuned through physical theoretical simulations (e.g. through the SCOPE RTM), the term hybrid model is referred to (Verrelst et al., 2019). By integrating the principles of an RTM and the flexibility of ML, hybrid models can effectively retrieve biophysical properties (e.g. LAI, FAPAR) (Estévez et al., 2022; Reyes-Muñoz et al., 2022) and infer carbon fluxes (e.g. Wolanin et al. (2019)), nevertheless, they remain still unexplored for providing global TCF from the synergy of satellite data streams. Data-driven methods have the ability to handle large amounts of data and capture complex relationships between satellite observations and the variables aimed for prediction (Garbulsky et al., 2008). While these relationships may sometimes lack intuitive clarity, when integrated with physical models they emerge as a robust analytical instrument capable of effectively tackling nonlinear problems with novel datasets.

Based on these methodological strategies and the above-published progress in TCF estimation, the following ongoing trends are worth mentioning: (1) a shift from discrete spectral band approaches (e.g. VIs) towards models trained with the full-spectrum information (Verrelst et al., 2019); (2) a tendency from linear models (e.g., LUE models) towards data-driven, nonlinear ML models (e.g., Tramontana et al., 2020); (3) a shift from desktop-based towards cloud-computing processing such as Google Earth Engine (GEE) (Gorelick et al., 2017). Review studies further identified the need for the estimation of uncertainties (Jung et al., 2020). Only a few TCF products provide uncertainties, e.g., utilizing bootstrapping ensemble models (Wild et al., 2022; He et al., 2022; Zhang and Ye, 2022). Additionally, synergies between missions should be exploited to enhance the monitoring of vegetation through diverse spectral domains and techniques. These methods could include measuring the optical reflectance or SIF emission of terrestrial vegetation (De Grave et al., 2020; Berger et al., 2022). Therefore, the synergy of S3 and S5P (S3&S5P) arose as an opportunity to study TCF through high-level products of VT, acquired at the original S3 Ocean and Land Color Instrument (OLCI) resolution of 300 m, besides the SIF information provided by TROPOMI. This combination will allow us to present an alternative to the widely used MODIS data that has long passed its expected design lifetime, and explore prototype models to be adapted for the upcoming FLEX mission.

The primary objective of this study is to develop globally applicable models for retrieving terrestrial carbon fluxes (TCFs), specifically GPP and NPP with associated uncertainties. To achieve this, we will employ a hybrid approach that combines SCOPE simulations with Bayesian machine learning prediction. This approach is necessary to account for the complex relationships between physical processes and TCFs. Gaussian process regression (GPR), a non-linear kernel-based ML method, will be employed to implement TCF models (Rasmussen and Williams, 2006). As a long-term goal, these hybrid models will be tailored and integrated into forthcoming FLEX-S3 processing chains, thereby enhancing the accuracy and reliability of TCF estimates from FLEX-S3 SIF observations.

2. Material and methods

Entering the post-MODIS era and with the ambition to explore alternative new-generation satellite data sources and products (i.e., solely based on ESA missions), as well as to introduce novel methodological

concepts into the production of TCF estimations (i.e., GPP, NPP), we present a workflow that fulfils the following criteria: (1) moving beyond spectral indicators (VIs), i.e. exploitation of quantitative VT as retrieved from S3-OLCI radiance data (Reyes-Muñoz et al., 2022); (2) introduction of a Bayesian ML algorithm in hybrid TCF modelling that explicitly provides uncertainty estimates; (3) ensuring that these models are physically sound by training through meaningful RTM SCOPE simulations; (4) analysing the contribution of TROPOMI SIF data as surrogate SIF data in preparation for the upcoming FLEX mission; and (5) introduction of GEE cloud-computing processing so that the workflow is fully scalable for any location or time window given the availability of the satellite data. Pursuing this research line, the main steps followed for mapping TCF variables at a global scale are schematized in Fig. 1 and detailed in the following sections.

2.1. Hybrid modelling strategy

Anticipating the non-linear relationships between SIF and TCF, given the dynamic photosynthetic activity and canopy heterogeneity, e.g., as outlined in Verrelst et al. (2016c), Magney et al. (2020), this study builds on the nonlinear Bayesian principles of GPR (Rasmussen and Williams, 2006). We pursued a hybrid workflow for quantifying TCF products at a global scale (Fig. 2), outlined as follows: (1) First, the SCOPE model (version 1.7, (Tol et al., 2009b)) was used for generating a training database for GPR to build retrieval models of GPP and NPP. The final models, named SCOPE-GPR-TCF, were designed to run with satellite-based products and climatic reanalysis model data embedded in GEE, specially intended to estimate global TCF over diverse land cover surfaces (e.g., broad leaf forests, crops, grasslands and wetlands). Second (2), the generated SCOPE-GPR-TCF global products were then validated against flux-tower observations, and also compared against reference satellite TCF products relying on process and LUE principles.

2.2. GPR algorithm

GPR was chosen as the core ML algorithm for predicting TCF given its excellent predictive power and provision of associated uncertainties (e.g., Verrelst et al., 2012a,b). In short, GPR approximates the relationship between input samples $x \in \mathbb{R}^D$ and output observations $y \in \mathbb{R}$ as $y = f(x) + \epsilon$, being ϵ an additive Gaussian noise with zero mean and variance σ_n^2, and $f(x)$ a Gaussian distributed random vector with zero-mean and Covariance matrix $\mathbf{K(x, x)}$ (Rasmussen and Williams, 2006). The algorithm uses a kernel function $\mathbf{k(x_i, x_j)}$ for solving $\mathbf{K(x, x)}$. The mean estimate results as:

$$f(x_*) = k_\star^T \alpha \tag{1}$$

with $f(x_*)$ the prediction at the x_* point and $k_\star^T$ the vector of covariances between the training and the incoming input x_* points; α is a vector quantifying the sample weight. The kernel used here is of type asymmetric square exponential, proved optimal for studies on earth observation, (Camps-Valls et al., 2016). Additionally, GPR model uncertainties (σ) are calculated by following the workflow presented in Reyes-Muñoz et al. (2022). In short, σ is calculated as the standard deviation of the posterior distribution function, which in turn depends on the prior distribution defined on initial assumptions, the reference observations y' and the likelihood function based on the Bayes theorem (Rasmussen and Williams, 2006). The mathematical expression to solve σ is defined as:

$$\sigma_f(x_*) = \sqrt{k(x_\star, x_\star) - v^T v} \tag{2}$$

where $k(x_\star, x_\star)$ indicates the kernel function calculated at the new input $x_\star$; v the vector $v = L \backslash k_\star$; L the low-triangular matrix calculated from the expression: $K + \sigma_n^2 I_N$, with $\sigma_n{}^2$ the noise variance and I_N the noise identity Matrix.
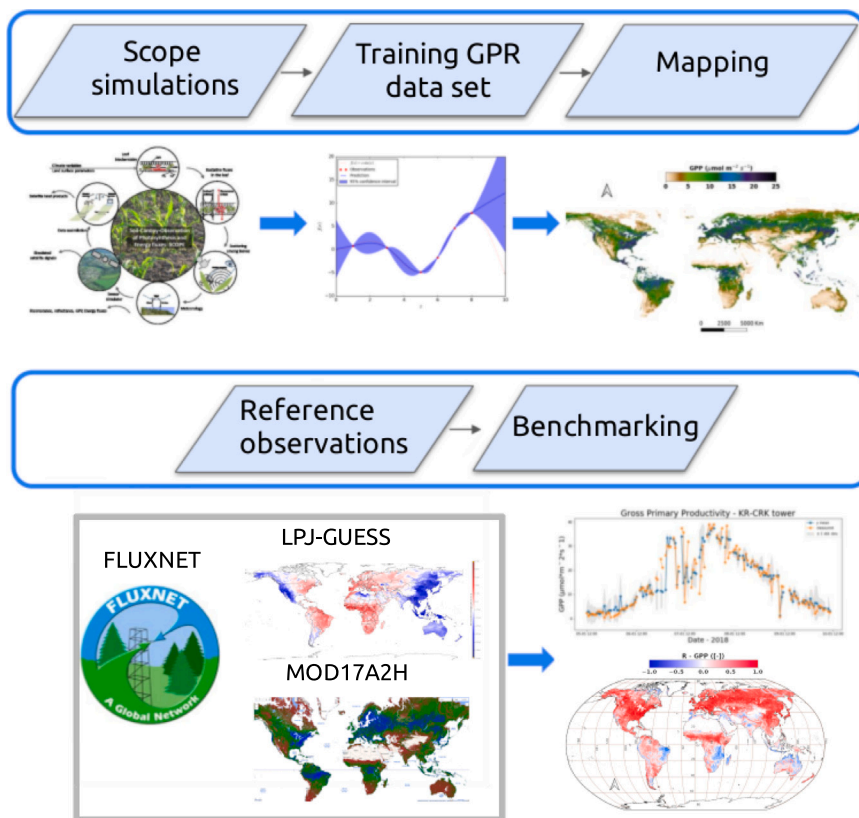
Fig. 1. Steps followed for training and mapping the models of TCF in the first stage, and validating the outcomes with reference products both at a local and global scale, in a second stage.
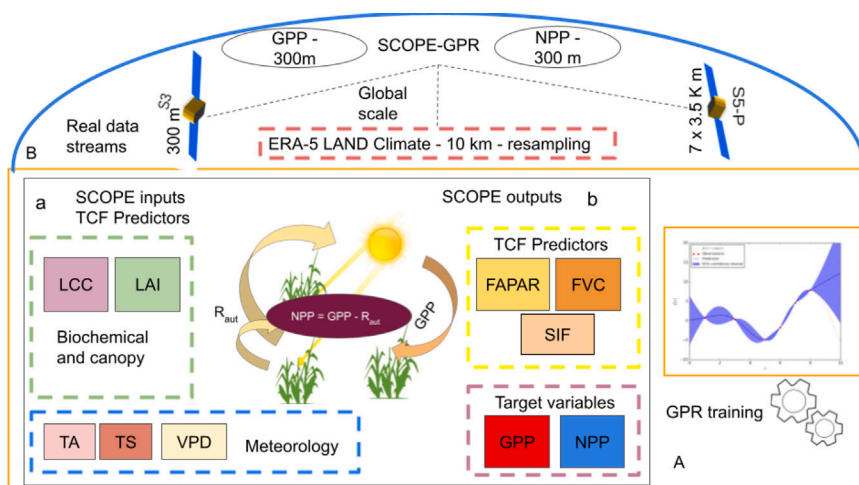

Fig. 2. Study of TCF: (A) The SCOPE RTM was used to simulate TCF, SIF, FAPAR and fractional vegetation cover (FVC), as a function of key inputs such as leaf chlorophyll content (LCC), LAI and meteorological variables. Training datasets of these variables were used for building TCF models. Global analysis of GPP and NPP was achieved in (B) at a spatial resolution of 5 km, increased to 300 m on specific regions of interest (ROIs), with climate data coming from the ERA5-LAND reanalysis models and satellite-based products of vegetation in (A). The spatial resolutions of the used input products for the predictions are also indicated.

The algorithm implemented in GEE is based on matrix calculations (through GEE Image-array objects), following the approach of Pipia et al. (2021), Reyes-Muñoz et al. (2022).

2.2.1. SCOPE-GPR-TCF models

A total of 2000 SCOPE simulations were run covering the widest variability of a set of considered input variables to reflect global conditions. Besides, the parameterization was defined according to previous studies focusing on global estimations and experiences of the authors (Asner et al., 2003; Fernandes et al., 2003; Berger et al., 2018; Wolanin et al., 2019; Prikaziuk et al., 2023). Table 1 provides detailed information on the simulation configurations. A random subsampling strategy was applied to reduce the simulation size to 2000 from the total number of combinations. Hereby, a wide set of variables, including the categories of biochemical, leaf, canopy or meteorology compose the

inputs of SCOPE, while FAPAR, FVC, SIF, GPP and NPP, and spectral reflectance (400–1020 nm) are SCOPE outputs, among others (Tol et al., 2009a; Hu et al., 2018). We have maintained some variables constant to keep the training data set as small as possible for a trade-off between performance and efficiency, for instance, leaf dry matter content, atmospheric pressure or canopy height. With the same purpose, the photosynthesis pathway here selected was C3, corresponding to the larger proportion of vegetation species around the world, predominant in forests and some of the most abundant croplands (e.g., wheat) (Still et al., 2003).

The selected input variables, i.e., predictors can be incorporated within the workflow for predicting TCF through satellite products and climatic reanalysis models. These predictors included: leaf chlorophyll content (LCC), LAI, FAPAR, FVC, shortwave incident radiation (SW), air temperature (TA), vapour pressure (EA) and SIF (see also Table 1). This selection relied on the availability of these variables from satellite data and climatic reanalysis models, either directly (SIF from S5P; SW, TA, EA from ERA5-LAND) or as here retrieved products (i.e., LCC, LAI, FAPAR and FVC from S3-OLCI); see Section 2.3 for details. The selection of the canopy and leaf variables (LAI, FAPAR, FVC and LCC) may raise the question of high similarity in terms of vegetation information. Note that the variables are highly related to green vegetation, but they provide specific differences. For instance, LAI is a measure of the physical structure of the canopy, while LCC and FAPAR are measures of the physiological function of the canopy. FVC, being closely related to LAI, provides an additional indication of vegetation density. See also the detailed discussion in Reyes-Muñoz et al. (2022).

The SCOPE-GPR-TCF models were created within the Automated Radiative Transfer Models Operator (ARTMO) toolbox (Verrelst et al., 2012c). Through ARTMO's machine learning regression toolbox (MLRA), GPR hybrid models were trained based on the eight selected input variables simulated by SCOPE, targeting GPP and NPP (Rivera-Caicedo et al., 2014). The SCOPE-GPR-TCF tuned hyper-parameters were then exported into GEE following the steps on https://github.com/msalinero/ARTMOtoGEE (accessed on 3rd July 2023). Lightweight models were targeted as a trade-off between performance and matrix computation memory limitations, given the special prediction suitability of GPR models trained with small sample sizes. The models were constructed by randomly selecting 300 samples for training from a total of 2000 simulations, while the remaining 1700 samples were utilized to evaluate the model's performance. A similar strategy was followed by Pipia et al. (2021), Estévez et al. (2022), Reyes-Muñoz et al. (2022), Salinero-Delgado et al. (2022). This process was repeated three times, with a different random sample selection in each iteration. The final model was chosen based on the highest scores achieved by the models during evaluation. The trend of model performance vs. the number of samples is shown in appendix Fig. A.5.

In an attempt to quantify the relative importance of the input variables simulating GPP and NPP in SCOPE and in the final SCOPE-GPR-TCF models, we applied: (1) a global sensitivity analysis (GSA) to SCOPE (SCOPE-GSA), informing about the relative contribution of all the input variables involved in the SCOPE simulations and driving the GPP and NPP outputs. The SCOPE-GSA employed a Saltelli variance-based calculation (Saltelli, 2004). Note hereby that it was not possible to include FAPAR, FVC, and SIF in the GSA, as they were outputs of SCOPE. (2) Subsequently, the key drivers out of the eight selected predictor variables of the final SCOPE-GPR-TCF models were inferred. An attractive property of GPR is its feature ranking of the contributing inputs of the models by using the automatic relevance determination (ARD) covariance function (Verrelst et al., 2016b). This automated feature ranking was derived from the built models, and the rankings were then presented into polar plots according to Ayala Izurieta et al. (2022) revealing the key driving predictors of the hybrid models. The polar plot represents a scaled function assigning a higher coefficient to more relevant predictors (or variables). The analysis will be further referred to as GPR-rank.

2.3. Input data for real-world application: S3&5P and ERA5 products

The satellite products used as predictors of the SCOPE-GPR-TCF models are listed in Table 2. (1) Prototype level-3 (L3) vegetation variables (LCC, LAI, FAPAR and FVC) come from the in-house developed and validated S3-derived products (Reyes-Muñoz et al., 2022) and are retrieved directly from top-of-atmosphere (TOA) observations of the S3-OLCI instrument. These retrievals are likewise obtained through hybrid SCOPE-based GPR models that run on S3-OLCI L1B radiance data in the spectral range between 400 nm to 1020 nm. By implementing the models into GEE, these products proved to be globally applicable, and intra-annual comparison against related MODIS and Copernicus products evidenced its spatiotemporal consistency (Kovács et al., 2023). Their implementation into GEE further enables running these models on spatial scales and time windows defined by the user.

(2) The satellite SIF data, so-called TROPOSIF, came from the TROPOMI observations (Veefkind et al., 2012). TROPOMI, aimed at monitoring atmospheric composition, is equipped with four spectrometers measuring the spectral range between 270 nm to 2385 nm. The TROPOSIF data are provided as ungridded L2 (satellite overpass) and L2B daily aggregations, obtained by a data-driven strategy from TOA radiance data in the far-red spectral region measured by TROPOMI (Guanter et al., 2021). Baselines TROPOSIF retrievals are focused on the 743–758 nm windows, meanwhile, a secondary dataset covers an extended range of 735–758 nm. Here, only the baseline TROPOSIF retrievals were tested. The SCOPE-GPR-TCF were trained to respond to SIF emitted in the same spectral range. Therefore, SIF was simulated through SCOPE over the 743–758 nm windows. The TROPOSIF daily-aggregated retrievals are scaled from TROPOMI observations (overpass at 13:30 mean local solar time) through a daily-length scale factor. The data were directly downloaded from http://ftp.sron.nl/open-access-data-2/TROPOMI/tropomi/sif/v2.1/l2b/ (accessed on 30th June 2023).

(3) For the weather data inputs, we used weather-climate data produced by the ECMWF ERA5-Land reanalysis models (Hersbach et al., 2020) i.e., shortwave incident radiation, air temperature, and vapour pressure. ERA5-Land produces estimates of atmospheric and land-surface variables by assimilating observations into physical equations. The data are offered globally in hourly, daily, or monthly aggregations at a horizontal resolution of 0.1° x 0.1°.

2.4. Spatiotemporal mapping

The SCOPE-GPR-TCF models were used for mapping from regional to global scales. Additionally, we focused on the Iberian Peninsula to prove GPP at a maximal spatial resolution of 300 m over a diversity of ecosystems belonging to different climatic regions (Kottek et al., 2006). To produce the 300 m resolution maps, coinciding with the OLCI original resolution, SIF data were gridded and resampled to 300 m from its original 7×3.5 km sounding footprint. Eq. (3) was used for GPP and NPP mapping as a function of the predictor vector composed of the eight independent variables (X). A range of temporal aggregations was applied for mapping GPP and NPP, from instant scenes (on 16th June 2019 at 13:30 pm) to annual values (2019). A common format based on 8-day-aggregated intervals was set for time series analysis of GPP and NPP and further cross-comparisons will be achieved with 8-day-aggregated reference products. Consequently, the predictors were averaged over 8 days. Also, the S3-derived VT predictors were found to be more robust beyond daily temporal resolution (Reyes-Muñoz et al., 2022), and therefore 8-days-aggregated VT were also used for instant retrievals of GPP and NPP. SIF L2 scenes were used for instant retrievals and the L2B daily product to process 8-day means (by averaging daily SIF values over 8 days). Hourly ERA5-Land meteorological data (i.e., SW, TA and EA) were used, both for instant retrievals and 8-day means. Thus, the instantaneous predictions of TCF is based on the combination of 8-day S3-derived VT, the instantaneous capture of

Table 1

Variable ranges used to obtain the simulated dataset through SCOPE, aimed at building the global GPP and NPP models. Note that only variables indicated in bold were applied for generating the final SCOPE-GPR-TCF models. In addition, the three SCOPE output variables also used as predictors are given. Target variables GPP and NPP are given as well (italics).

	Variable (unit)	Symbol	Min - Max	n samples	Distribution
Meteorological variables	**Shortwave incident radiation** (W m^{-2})	**SW**	0 - 1400	100	Uniform
	Air temperature (° C)	**TA**	−10–50	60	Uniform
	Atmospheric pressure (hPa)	AP	970	–	Constant
	Carbon dioxide concentration (ppm)	CO_2	380	–	Constant
	Oxygen concentration (ppm)	O_2	209	–	Constant
	Vapour pressure (hPa)	**EA**	0–150	15	Uniform
Leaf variables	Water thickness (cm)	C_w	0 - 0.5	5	Uniform
	Leaf structure parameter (-)	N	1.4	–	Constant
	Leaf dry matter content (g cm^{-2})	C_m	0.012	–	Constant
	Leaf carotenoid content (μg cm^{-2})	C_{xc}	10	–	Constant
	Leaf chlorophyll content (μg cm^{-2})	**LCC**	0–100	20	Uniform
Leaf biochemical	Maximum carboxylation capacity (μmol m^{-2} s^{-1})	V_{cmax}	40–80	10	Uniform
	Ball–Berry stomatal conductance [-]	BSC	2 - 20	20	Uniform
	Extinction coefficient for V$_{cmax}$ [-]	ECV	0 - 0.8	8	Uniform
	Stress factor	SF	0–1	4	Uniform
	Photosynthetic pathway	PPW	C3	–	Constant
Canopy variables	**Leaf area index** (m^2 m^{-2})	**LAI**	0–8	30	Uniform
	Leaf inclination distribution function	LIDF	−1 - 1	10	Uniform
	Leaf width (m)	LW	0.1	–	Constant
	Vegetation height (m)	h_c	10	–	Constant
	Soil boundary layer resistance (s m^{-1})	SBLR	10	–	Constant
	Leaf boundary resistance (s m^{-1})	LBR	10	–	Constant
SCOPE output	**Solar-induced fluorescence** (W m^{-2} μm^{-1} sr^{-1})	**SIF**			
	Fraction of absorbed photosynthetically active radiation [-]	**FAPAR**			
	Fractional vegetation cover [-]	**FVC**			
Target variables:	*Gross primary productivity* [μmol m^{-2} s^{-1}]	*GPP*			
	Net primary productivity [μmol m^{-2} s^{-1}]	*NPP*			

Table 2

Overview of the products used as real data-streams inputs (i.e., the eight predictor variables) for SCOPE-GPR-TCF models.

Product	Predictor variables	Source	Spatial res.	Temporal res.	Method
S3-derived VT	**LCC, LAI, FAPAR, FVC**	S3-OLCI (L1C)	300 m	daily (S3A + S3B)	hybrid (GPR, SCOPE)
ERA5-LAND	**TA, SW, EA**	ECMWF	0.1°	hourly–monthly	climate reanalysis
TROPOMI-SIF	**SIF$_{743-758}$**	S5P-TROPOMI (L2)	7 × 3.5 km	daily	spectral fitting function

SIF (at the S5P overpass time) and hourly ERA5-LAND data. Higher aggregation levels (e.g. annual) of GPP and NPP were produced from the 8-day GPP and NPP products.

$$y_h = f(x^D)$$
$$+ \epsilon; x^D : \left(X_{8d}^{LCC} \ X_{8d}^{LAI} \ X_{8d}^{FAPAR} \ X_{8d}^{FVC} \ X_{h}^{SW} \ X_{h}^{Ta} \ X_{h}^{ea} \ X_{h}^{SIF_{743}} \right)$$
(3)

$$y_{8d} = f(x_{8d}{}^D)$$
$$+ \epsilon; x^D : \left(X_{8d}^{LCC} \ X_{8d}^{LAI} \ X_{8d}^{FAPAR} \ X_{8d}^{FVC} \ X_{8d}^{SW} \ X_{8d}^{Ta} \ X_{8d}^{ea} \ X_{8d}^{SIF_{743}} \right)$$
(4)

Furthermore, we incorporated an analysis to assess the significance of the different predictors for mapping applications. Regional mapping will be conducted with TCF models including all predictors and removing predictors one by one. This comparative approach will enable us to evaluate the contribution of the different variables, as anticipated from the S3-FLEX tandem, in regional (to global) TCF retrieval.

2.5. Validation and benchmarking

Our objective was to deliver reliable SCOPE-GPR-TCF models globally while also maintaining their reliability at the local scale. To evaluate this, spatiotemporal cross-comparisons against reference products were performed at various spatial scales. First, the SCOPE-GPR-TCF mapping results were compared to ground measurements from the FLUXNET network (Pastorello et al., 2020; Delwiche et al., 2021).

FLUXNET, a global network of eddy covariance (EC) flux towers, provides estimates of carbon fluxes between the biosphere and the atmosphere. The product includes samples of NEE (CH_4 and CO_2) and meteorological data either measured by the towers or modelled through ERA5-Land at the location points. It also includes GPP data obtained through daytime-based partition methods (Lasslop et al., 2010).

We selected 113 towers providing data over the year 2019, located on distinct land cover types over Europe and America, as shown in Fig. 3. We used the Integrated Carbon Observation System (ICOS) (Paris et al., 2012) and the AmeriFlux site to access the quality-controlled L2 data, updated until the year 2022 through the sites https://www.icos-cp.eu/data-products and https://ameriflux.lbl.gov/ respectively (accessed on 1st December 2023).

Next, for the global benchmarking of the models, we used the LPJ-GUESS process-based model (Martín Belda et al., 2022) and the MOD17A2H-8-days (Running et al., 2015) products. Table 3 summarizes the original formats. LPJ-GUESS was chosen due to its global coverage at an increased spatial resolution with regard to other process-based models (e.g. ORCHIDEE), capturing better spatial heterogeneity. We also chose the MOD17A2H product (which uses the LUE concept) that has a spatial resolution close to the one provided by S3. Both products were freely available at the temporal windows used in our analysis. We resampled the SCOPE-GPR-TCF products to meet the corresponding spatial resolutions of the reference products. In the case of the LPJ-GUESS product, we downloaded hourly global GPP estimations at a spatial resolution of 0.5° from the ICOS site. These data were aggregated in 8-day steps (averaging hourly observations over 8 days) for the year 2019 to study the intra-annual temporal correlation with SCOPE-GPR-TCF through the Pearson correlation coefficient (R). The

Table 3

Spatiotemporal resolution of the original products (GPP and NPP) used for benchmarking over the year 2019.

Product	Spatial–temporal resolution	Temporal resolution for benchmarking
MOD17A2H	500 m/8 days	8 days/monthly
FLUXNET	local point/hourly	8 days
LPJ-GUESS	0.5/hourly °	8 days
SCOPE-GPR-TCF	300 m/hourly	8 days/monthly
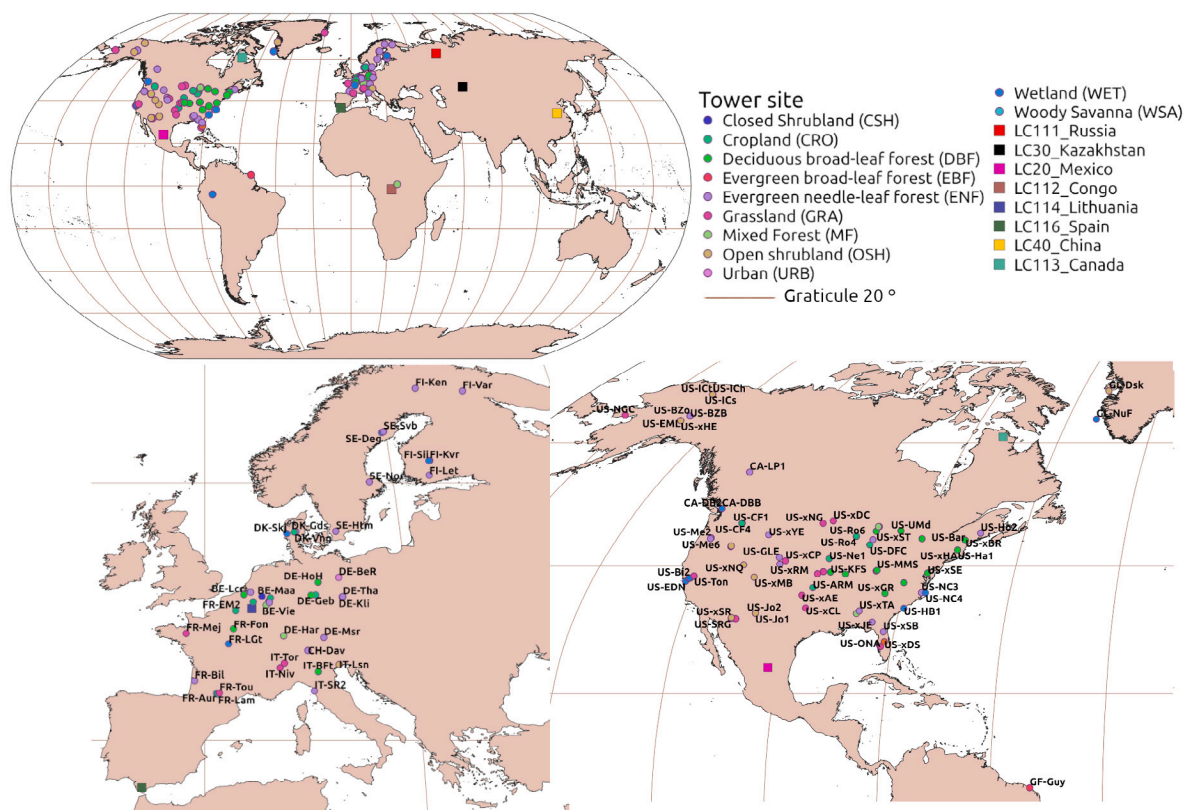
Fig. 3. Locations of the flux towers measuring carbon fluxes (circles) and singular land cover types (squares) where the SCOPE-GPR-TCF results were analysed. The tower codes are displayed next to the locations.

MOD17A2H-8-days GPP/NPP product was accessible directly from the GEE platform. The SCOPE-GPR-TCF estimations aggregated to eight days were produced through Eq. (4).

Further, we studied the spatiotemporal correlation of SCOPE-GPR-TCF against MOD17A2H on specific land covers selected through the "Copernicus Global Land Cover Layers" (Buchhorn et al., 2020). We focused on the areas plotted in Fig. 3 and listed in Table 4. The forest areas presented tree canopy covers denser than 70%.

Finally, monthly composition maps were produced to study the spatial correlation between SCOPE-GPR-TCF and MOD17A2H in June 2019. This period presented a good availability of data, given that for some northern regions (e.g., Tundra) all satellite data appeared to be unavailable in winter.

3. Results

3.1. Performance of the SCOPE-GPR-TCF predictors

The importance of the selected predictors has been analysed at two different stages. In the first stage, we applied the SCOPE-GSA to the selected input variables used to run the SCOPE simulations. In the second stage, we analysed the importance of the predictor's vector within the trained GPR models through the GPR-rank.

Fig. 4(a) expresses the explained variance of the targeted SCOPE outputs (GPP and NPP) as a function of the considered input variables (see Table 1) through the first-order sensitivity index (S1) as blue bars, and the total sensitivity index (ST) as red bars. S1 represents the relative contribution of a single input variable to the variance of the model output without considering interactions with other variables. In contrast, ST considers the interaction with the other variables. For ST, the plots show a prominent influence of SW = 34% (43%), LAI = 28% (19%), V_{cmax} = 22% (15%) and LCC = 11% (13%). BSC stands out by its remarkable relative predictive strength (GPP and NPP) with an S1 = 25%, in contrast with a low value of ST = 0.5%, revealing a low influence alongside the other variables. V_{cmax} also presents sharp divergences between S1 and ST for NPP (32% and 15% respectively) as well as for GPP in opposite weight (5% and 22%). The contrasting behaviour of S1 and ST suggests that there are significant interaction effects between several variables (V_{cmax}, BSC, SW). For instance, V_{cmax} is strongly related to LCC, leading to this effect (Croft et al., 2017). However, more in-depth analysis would be required to confirm, which, however, goes beyond the scope of the study. The other variables play only a marginal role in explaining the variance of GPP and NPP.

Table 4

Selected land cover types with codes, extensions and biomes for spatial and temporal benchmarking with MOD17A2H, identified through the "Copernicus Global Land Cover Layers". Biome classification by Olson and Dinerstein.

Code	Land cover	Extension (ha)	Biome
LC111	evergreen needle-leaf forest	3,666,086.67	Taiga
LC112	evergreen broad-leaf forest	2,153,746.44	Tropical rainforest
LC113	deciduous needle-leaf forest	407,769.25	Tundra
LC114	deciduous broad-leaf forest	36,364.56	Temperate forest
LC116	evergreen broad-leaf forest	84,159.79	Mediterranean forests, woodlands and scrub
LC40	crop land	84,159.79	Grass land
LC20	shrubland	168,621.02	Grassland
LC30	grassland	429,633.84	Grassland
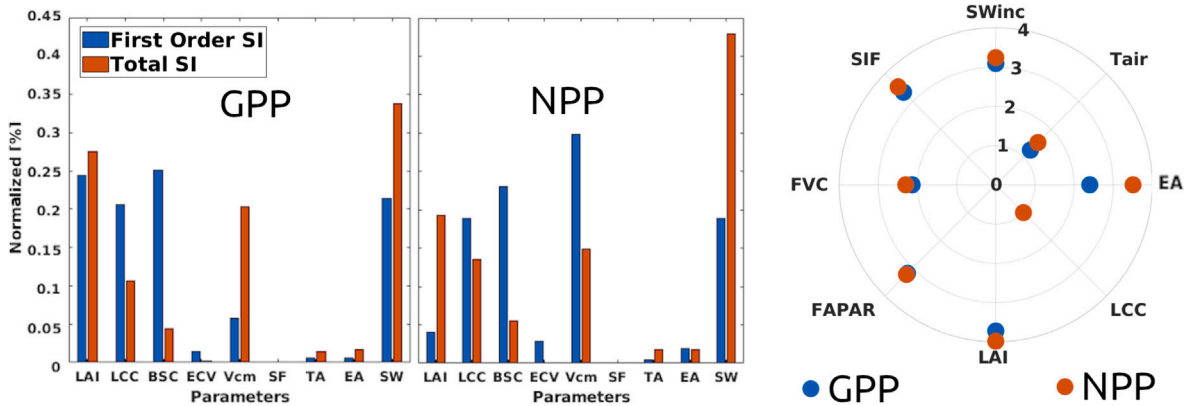
Fig. 4. **(a)** GSA of input variables for SCOPE simulations (SCOPE-GSA): GPP (left) and NPP (middle). **(b)** Polar plot of the predictor relevance of GPR predictors (GPR-rank): GPP (**blue**), and NPP (**red**). (For interpretation of the references to colour in this figure legend, the reader is referred to the web version of this article.)
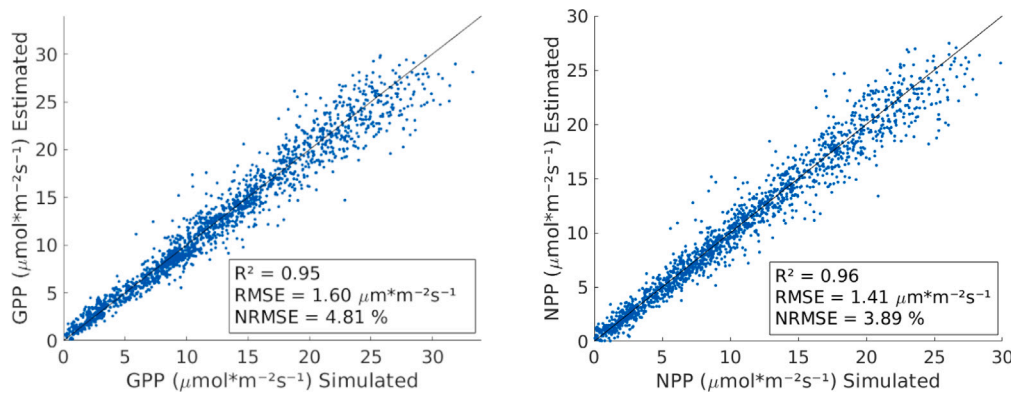
Fig. 5. Scatterplots of the theoretical performance of the SCOPE-GPR-TCF models based on the set of 8 predictor variables LCC, LAI, FAPAR, FVC, SIF, SW, TA and EA.

The bands' (predictors) rank of the tuned SCOPE-GPR-TCF models is quantified in the polar plot of Fig. 4(b). Predictors plotted outwards become more important. LAI scores the first position, followed by SIF, FAPAR, and SW. The analysis revealed the key drivers of TCF, which are critical for creating optimal SCOPE-GPR-TCF models.

The theoretical performances of the optimal SCOPE-GPR-TCF models, based on the set of 8 predictor variables LCC, LAI, FAPAR, FVC, SIF, SW, TA and EA, are shown in Fig. 5. High scoring was obtained for GPP and NPP with $R^2 = 0.95$ and 0.96; $rmse = 1.60$ μmol m^{-2} s^{-1} and 1.40 μmol m^{-2} s^{-1}, respectively.

3.2. Global and regional mapping

Strengthened by the highly accurate theoretical retrieval performance of the hybrid models, SCOPE-GPR-TCF models were subsequently fed with data streams from satellite products, such as the S3-derived VT (i.e., LCC, LAI, FAPAR, and FVC) and TROPOSIF from

S5P, as well as the climatic data from ERA5-Land products. Global GPP and NPP maps were processed along with the model-based uncertainty σ (Fig. 6). GPP and NPP are given in a composition scene with the same solar local time (1:30 pm) across the world (Fig. 6, first and third rows) for the 16th of June 2019. The maps were produced with a spatial resolution of 5 km. Total annual GPP and NPP values (2019) are also shown in Fig. 6 (second and fourth rows). Finally, the annual standard deviations were also calculated (fifth and sixth rows) providing information about the spatial distribution of seasonality around the world. Overall, the maps reflect a consistent spatial distribution highlighting the biomes along a longitudinal–latitudinal gradient, including close forests, savannas, and scarcely vegetated areas. The principal forest regions present value ranges (instant captures on row (1) of 20–25 μmol m^{-2} s^{-1}, including the Taiga, the temperate, and the tropical forests. Moderate values between 5–10 μmol m^{-2} s^{-1} are found over the African Savanna, the Mediterranean forests, and the croplands around the globe (e.g. South America). Desert or scarcely vegetated
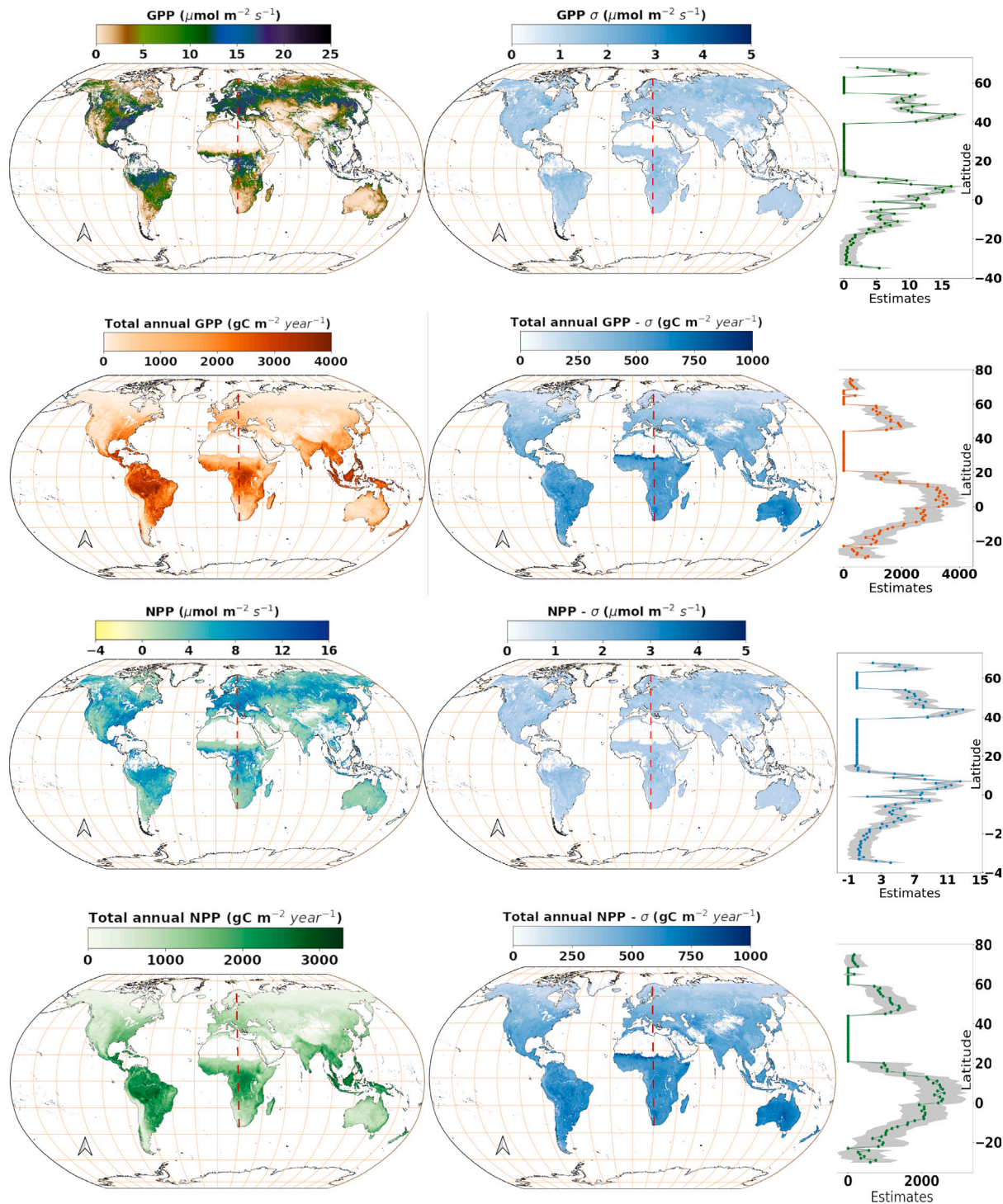
Fig. 6. TCF Global maps at 5 km using SCOPE-GPR-TCF models: by row (GPP and NPP on 16/6/2019 at 1:30 pm, total annual accumulated GPP and NPP in 2019, GPP and NPP annual standard deviations), by column mean values, corresponding uncertainties and profile at 20° longitude indicated by the red dashed line.

areas present values between 0–5 μmol m^{-2} s^{-1}. Annual accumulated maximum values of GPP around 4000 gC m^{-2} y^{-1} were reached on tropical forests (around 3200 gC m^{-2} y^{-1} in the case of NPP). The maps of standard deviations highlight the middle latitudes with maximum values, signifying greater seasonality (reaching up to 1800 gC m^{-2} y^{-1} for GPP and 1600 gC m^{-2} y^{-1} for NPP).

Estimates' spatial fidelity can be assessed by mapping associated uncertainties (σ). Maps of σ are provided (right), presenting values in the range between 0 and 5 μmol m^{-2} s^{-1} for the instantaneous scenes. The overall distribution tends to be quite uniform globally in all examples, following lightly a similar spatial pattern compared to the estimates (i.e., maximum deviations to be found in most green areas). Due to that σ presents globally a narrow variation range, the uncertainties relative to estimates are higher for areas with lower estimates. The relative σ oscillates regularly in the range between 10%–40% of the estimates.
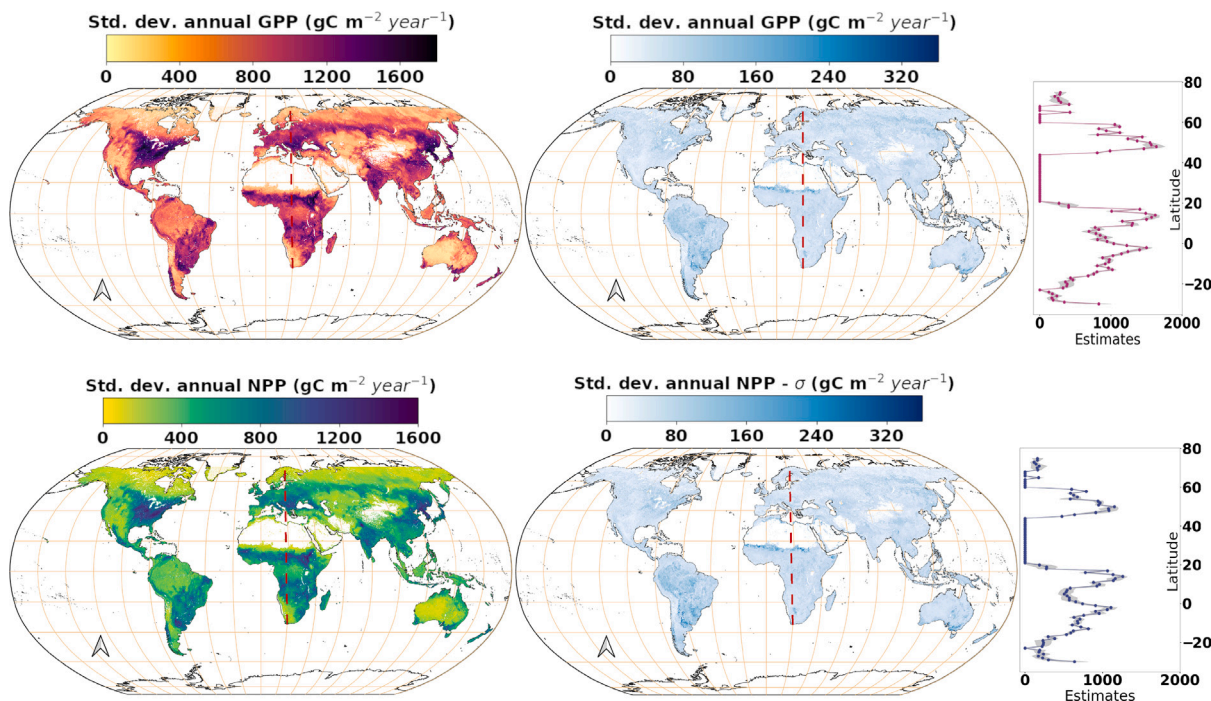
Fig. 6. (*continued*).

A latitudinal profile along the meridian at 20° is presented through the plots on the right side. Colour lines represent the estimates, while grey shadows correspond to uncertainties. These profiles all show a clear latitudinal transition, with two prominent peaks observed at the equator and middle latitudes (roughly 44°) for the instant captures on 16th June 2019. In contrast, annual accumulated values exhibit a single, distinct peak near the equator. Moreover, the standard deviations reach maximum values at 44° and 15°.

A closer inspection of the regional scale at the S3-OLCI original 300 m resolution is given in Fig. 7, focusing on the Iberian Peninsula for the 16th of July 2019. The Iberian Peninsula covers a diversity of surface types, with four climate types according to the classification made in Kottek et al. (2006). The detailed maps allow for visually exploring the spatial behaviour of our model both at 5 km (first row) and at native resolution of S3-OLCI (from second row) with the corresponding estimate (left) and uncertainty (right) layers. In an attempt to analyse the impact of the variables involved in the SCOPE-GPR-TCF models we present six models excluding each predictor one by one (under the second row). The Figure reveals next points:

(1) A smoothed spatial distribution is observed from the map at 5 km resolution (first row), coherent with the different climatic regions. (2) A sharper representation of land cover diversity is shown in the original model at 300 m (second row). In this case, the uncertainty layer hardly varies, and the potential improvements in σ due to a higher resolution may be balanced with the effect of resampling TROPOSIF. The map reflects ranging quantities of carbon rates captured by vegetation, with maximum values of 25 $\mu mol\,m^{-2}\,s^{-1}$ reached on closed and mixed forests as well as croplands (e.g., rice) dispersed over the Peninsula. (3) The retrieval of GPP removing the major predictors LAI and SW (and also LCC) is drastically underestimated for the whole territory. The impact is more pronounced when removing SW, with a mean difference of 4.09 $\mu mol\,m^{-2}\,s^{-1}$ (an underestimation of 68% in relative terms). Furthermore, the uncertainties increased between 0.1–0.2 $\mu mol\,m^{-2}\,s^{-1}$ on average. (4) The impact of SIF, in synergy with the S3-derived VT is revealed from the set of presented maps. The non-SIF version (third row) presented overestimated values with a mean and standard deviation of 4.25 and 1.55 $\mu mol\,m^{-2}\,s^{-1}$ higher than the version including all predictors (71% and 39% respectively, in relative

terms). The σ layer of the non-SIF model reveals a markedly irregular spatial distribution, highlighting a geographical diversity impacting the reliability of the model. Higher uncertainties appear often linked with scarce vegetated areas or managed crops in the first growth stages. According to these results, the role of SIF is especially notable for providing reliable estimates of the maximum and minimum values of TCF as well as a coherent spatial distribution. (5) The non-FAPAR and non-FVC models also exacerbated the results with regards to the version including all predictors, presenting nevertheless moderate deviations (especially lower in the case of the non-FVC model).

3.3. Validation of SCOPE-GPR-GPP with partitioned estimates at flux towers

To validate the global SCOPE-GPR-GPP model at the local scale, we compared temporal profiles of GPP at flux tower sites with GPP partition estimates provided by FLUXNET (see Fig. 3 to find locations). The 8-day steps evolution of GPP at the tower locations is delineated in Fig. A.6. The time series correspond to observations of the FLUXNET product and predictions made by the SCOPE-GPR-GPP model. The time window of the analysis ranged from 1st January 2019 until 31st December 2019. The validation is summarized in Fig. 8. The R^2 and *rmse* statistics were calculated for each tower and represented in the boxplots, grouped by distinct vegetation types (See Fig. 3 for definitions). Overall, the products present a close agreement across most ecosystems, with the best results of $R^2 = 0.9$ for a crop site (US-DFC) and *rmse* = 0.8 $\mu mol\,m^{-2}\,s^{-1}$ for a grassland site (US-Wkg). Regarding the median statistics in Fig. 8, the best position (excluding WSA with only 2 samples) corresponds to GRA (median $R^2 = 0.7$) and DBF (median *rmse* = 2.3 $\mu mol\,m^{-2}\,s^{-1}$). SCOPE-GPR-GPP and FLUXNET products are well correlated over the mean world forest types ENF, DBF, MF and OSH with R^2 medians around 0.6. Nevertheless, the correlation was found to be poor for EBF. In most cases, Figs. 8, and A.6 reveal that seasonality is well represented by SCOPE-GPR-GPP.

3.4. SCOPE-GPR-TCF global performance benchmarking

To evaluate the consistency of the global dynamics of SCOPE-GPR-TCF products we conducted spatiotemporal analyses with respect to
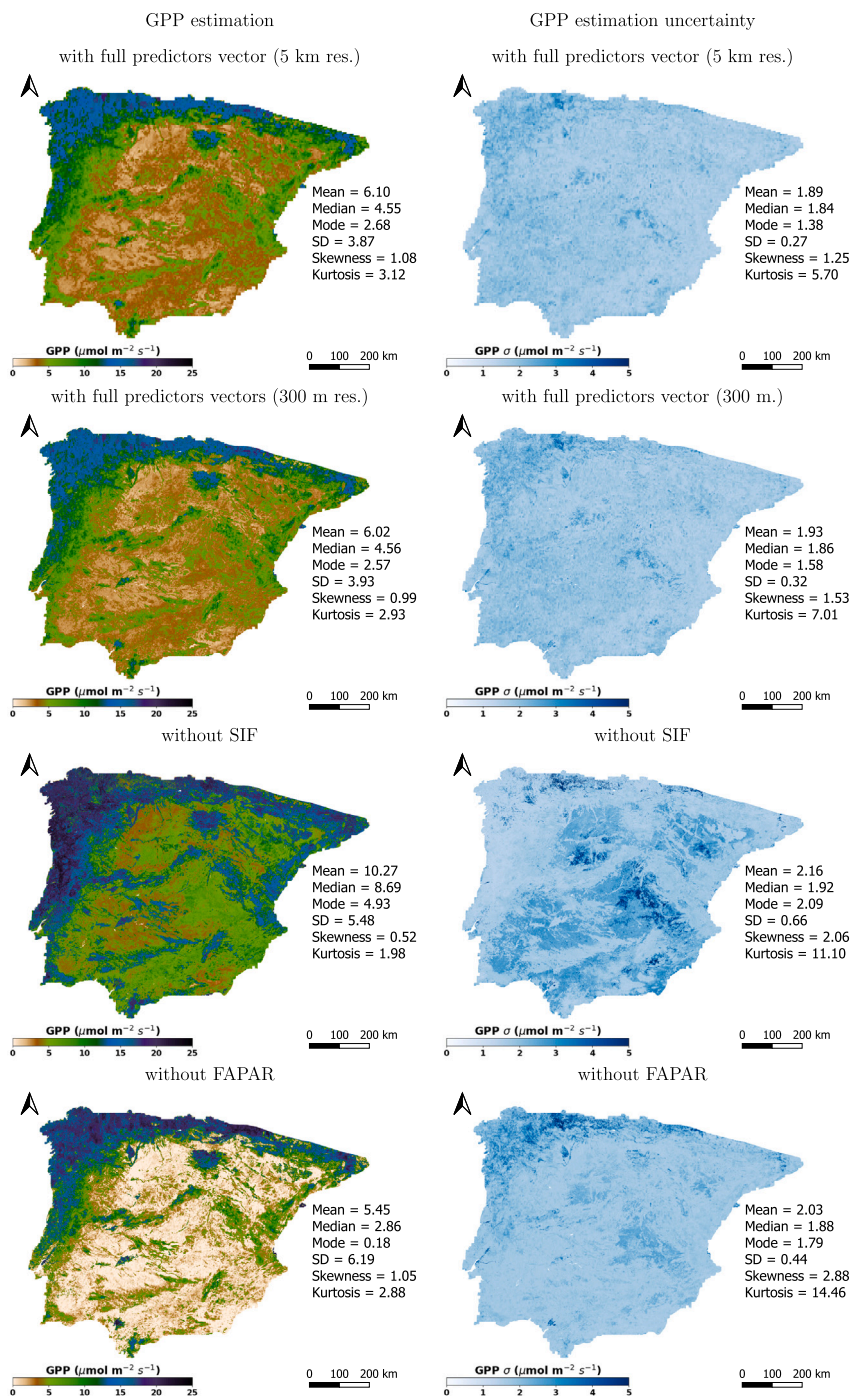
GPP estimation
with full predictors vector (5 km res.)

GPP estimation uncertainty
with full predictors vector (5 km res.)

with full predictors vectors (300 m res.)

with full predictors vector (300 m.)

without SIF

without SIF

without FAPAR

without FAPAR

Fig. 7. Regional maps (Iberian Peninsula) of GPP produced through SCOPE-GPR-TCF models for the date of 16th July 2019, including all the predictors (rows one and two at 5 km and 300 m spatial resolutions), and excluding other predictors one by one (from row three). Uncertainties are given at right.

reference products. First, a global-scale cross-comparison against LPJ-GUESS (GPP) and MODIS-MOD17A2H (GPP and NPP) is shown over time at spatial resolutions of 0.5° and 5 km respectively, and temporal steps of 8 days, calculating the intra-annual correlation coefficient (R) and the *rmse* per-pixel for the year 2019 (Figs. 9 and 10). Detailed analysis on different land cover types across the globe was carried out taking advantage of the higher spatial resolution of the MODIS product at 500 m (Figs. 11 and 12).

The intra-annual R coefficient between the SCOPE-GPR-TCF and LPJ-GUESS estimations (Fig. 9) resulted consistently, especially in the middle-high latitudes of the northern hemisphere and in parts of the tropical regions mainly composed of deciduous forests. Temperate

forests and Taiga arose as the big extensions presenting the highest correlations. Conversely, equatorial evergreen forests and other areas at low latitudes presented weak or negative correlations. The *rmse* shows smooth values for the same regions where high correlations were obtained, with typical values between 0 and 2 μmol m^{-2} s^{-1}. The equatorial evergreen forests presented the maximum *rmse* values. The histogram of correlation values indicates that most pixels follow a high correlation of 0.8, with maximums of 0.95 and minimums of -0.92. The *rmse* histogram indicates that the deviations between both models are more frequent around 1.93 μmol m^{-2} s^{-1}, with the sharpest discrepancies found in the Amazon region.

GPP estimation

without LAI

GPP estimation uncertainty

without LAI

Mean = 3.51
Median = 1.82
Mode = 0.15
SD = 4.17
Skewness = 1.17
Kurtosis = 3.35

Mean = 2.14
Median = 1.81
Mode = 1.76
SD = 0.81
Skewness = 2.32
Kurtosis = 8.50

without SWinc

Mean = 1.93
Median = 0.81
Mode = 0.05
SD = 2.66
Skewness = 1.29
Kurtosis = 3.70

without SWinc

Mean = 2.04
Median = 1.93
Mode = 2.18
SD = 0.41
Skewness = 3.08
Kurtosis = 16.62

without FVC

Mean = 7.04
Median = 4.82
Mode = 2.81
SD = 4.96
Skewness = 1.06
Kurtosis = 2.94

without FVC

Mean = 1.99
Median = 1.94
Mode = 1.76
SD = 0.30
Skewness = 1.19
Kurtosis = 5.39

without LCC

Mean = 3.29
Median = 1.71
Mode = 0.14
SD = 3.95
Skewness = 1.16
Kurtosis = 3.32

without LCC

Mean = 2.16
Median = 1.83
Mode = 1.82
SD = 0.82
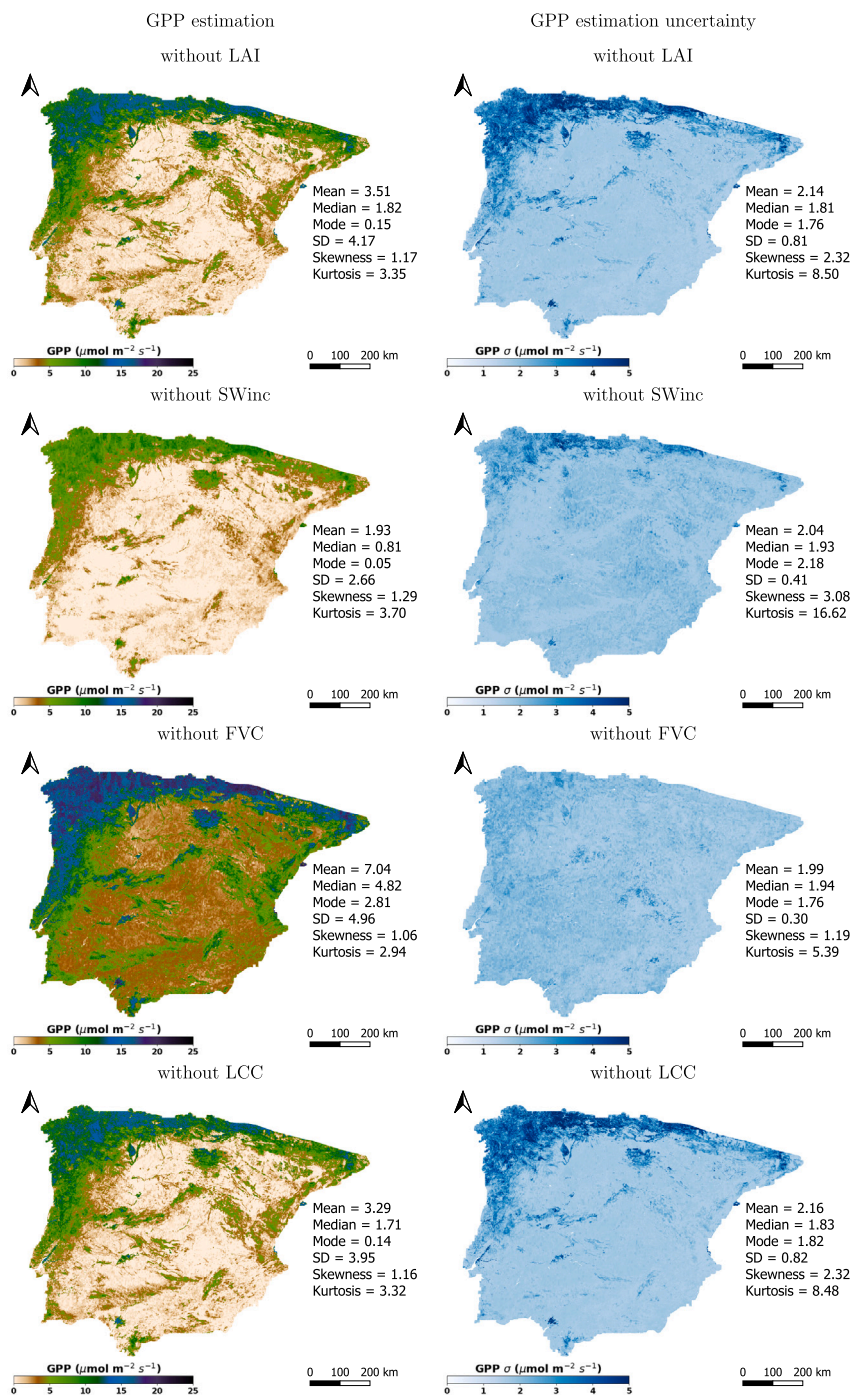Skewness = 2.32
Kurtosis = 8.48

Fig. 7. (*continued*).

The map of the intra-annual R correlation between SCOPE-GPR-TCF and MOD17A2H is shown in Fig. 10. Consistently with the analysis with respect to LPJ-GUESS (GPP), a good correlation emerged at northern and middle latitudes, meanwhile, weaker correlations are observed in the equatorial zone and desert areas (e.g., Australia, Namib desert). In comparison with LPJ-GUESS, correlations were found however higher both in the northern and southern hemispheres. In this case, a smoother spatial distribution of R is distinguished globally, with good performances across distinct biomes such as the Tundra, the Savanna, and the grasslands. The *rmse* maps between SCOPE-GPR-TCF and MOD17A2H (GPP and NPP) also show a smoother spatial distribution, with lower values, especially in the northern hemisphere. As in the case of the analysis with LPJ-GUESS, the higher values of *rmse* were obtained in the tropical regions (e.g., Amazon) with maximum values of 6 $\mu mol\,m^{-2}\,s^{-1}$.

The histograms indicate generally strong correlations, with the most frequent R values of 0.94 for GPP and 0.92 for NPP. The most frequent values of *rmse* were 1.26 $\mu mol\,m^{-2}\,s^{-1}$ for GPP and 1.05 $\mu mol\,m^{-2}\,s^{-1}$ for NPP. Overall, the histogram statistics indicate the existence of a moderate to good correlation globally between the dynamics modelled by SCOPE-GPR-TCF and by LPJ-GUESS and MOD17A2H.

A time series analysis for GPP and NPP in relation to MOD17A2H is given in Fig. 11 over the distinct experimental sites (squared locations in Fig. 3 and Table 4), for 8-days temporal steps. The observed temporal profiles depend on the land cover type. The correlation is low for evergreen broad-leaf forests (e), at the equator, due to mismatches along the strong intra-year variability and for the Tundra (f) where MOD17A2H start observing photosynthetical activity only from May–June. For the
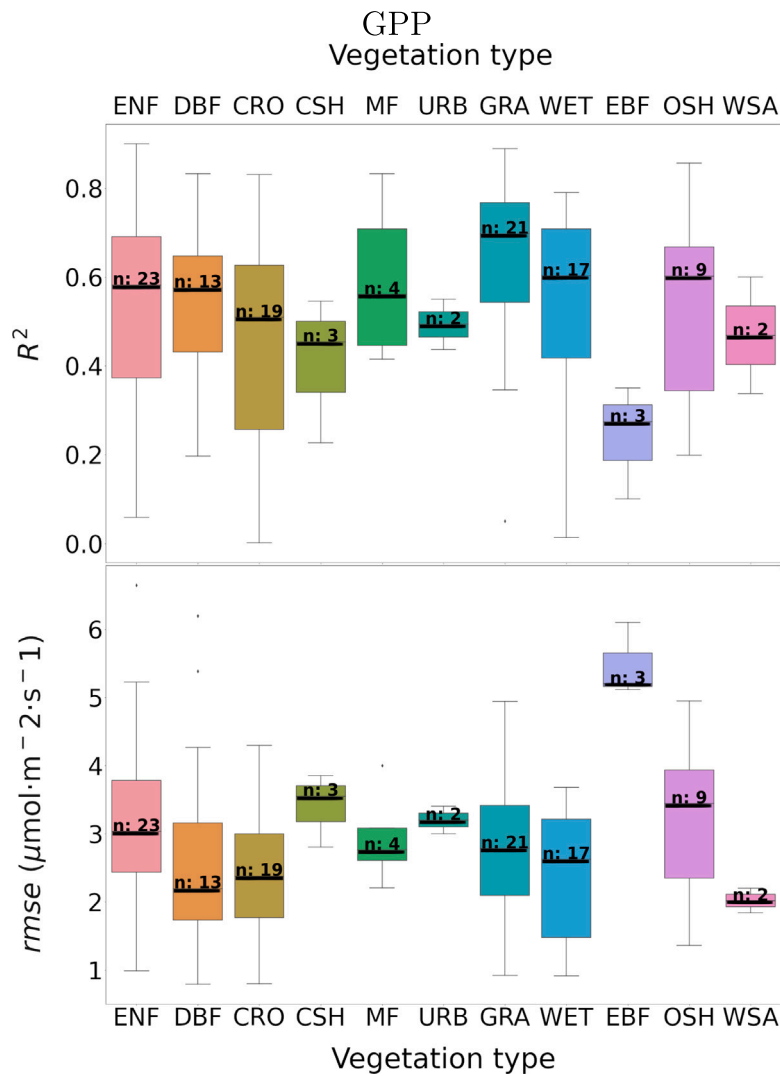
Fig. 8. Intercomparison of GPP estimations at 113 flux tower sites over Europe and America (R^2 (top) rmse (bottom)).
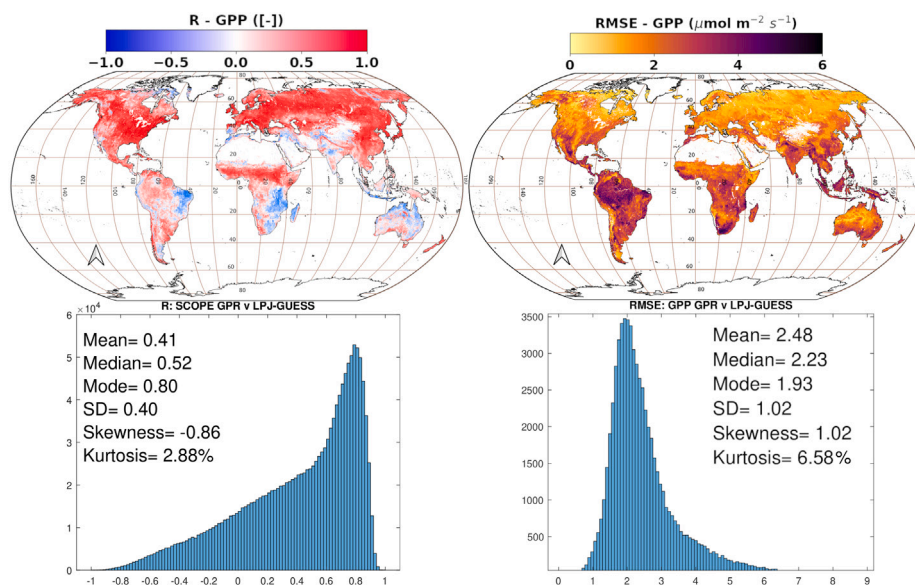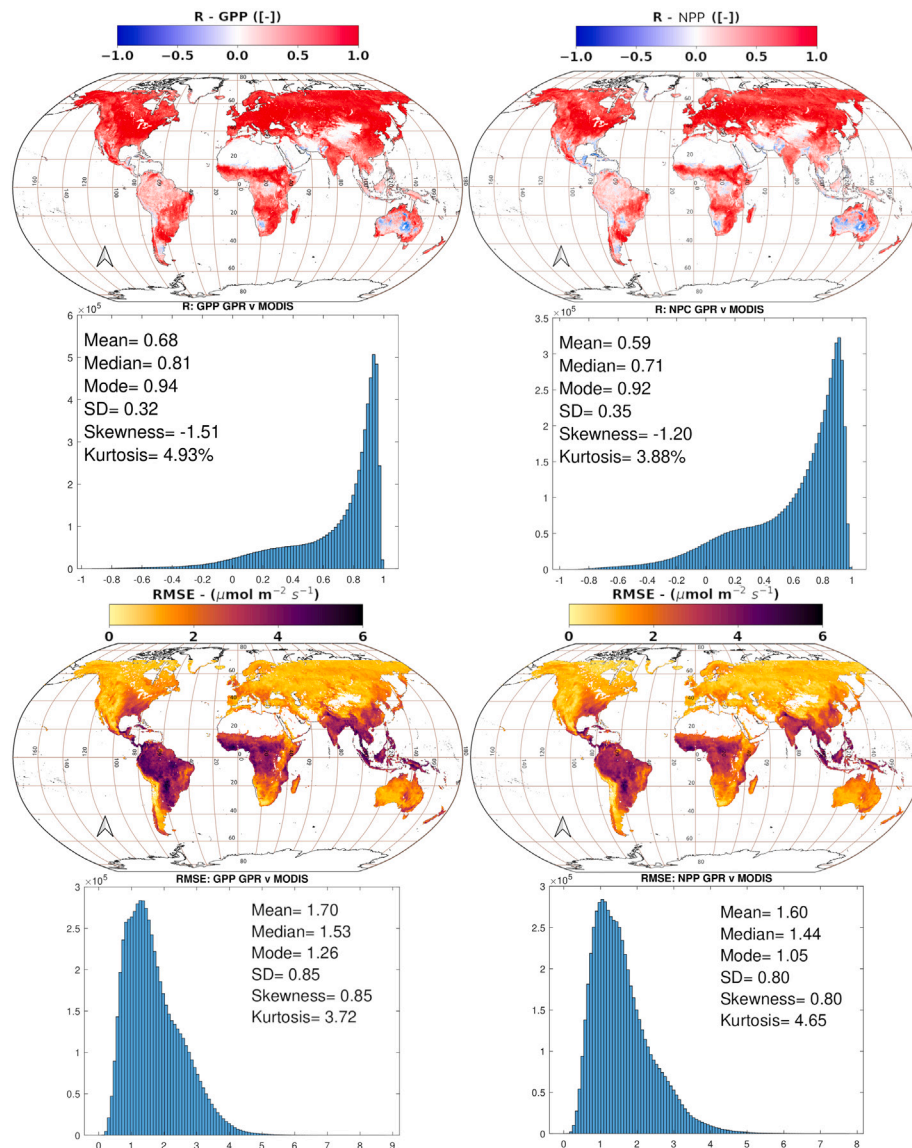

Fig. 9. Intra-annual R correlation (left) and *rmse* (right) between SCOPE-GPR-TCF and LPJ-GUESS data for GPP over the year 2019. Both datasets consisted of 8-days temporal steps of global products at a spatial resolution of 0.5°.

Fig. 10. Intra-annual correlation (R) and *rmse* against MODIS data for GPP (left) and NPP (right) over the year 2019. Both datasets consisted of 8-days temporal steps of global products at a spacial resolution of 5 km.

other cases, the R^2 ranges between 0.47 and 0.93 (corresponding with grasslands and evergreen needle-leaf forests respectively), and *rmse* in the range 0.21–4.17 μmol m^{-2} s^{-1} (for shrublands and croplands, respectively). The higher *rmse* emerged over the managed croplands in eastern China, with an overestimation of GPP and NPP relative to MOD17A2H, especially during the peak seasons.

Finally, the spatial correlation of SCOPE-GPR-TCF GPP and NPP with MOD17A2H estimations (R^2) and the distance (*rmse*) from pixel values is shown in Fig. 12. Comparisons are based on monthly composites of June 2019, and grouped by land cover category (see Table 4). The sample size varies between classes due to the different extensions of the experimental sites. In general, predictions move around ranges close to MOD17A2H observations (*rmse*), with moderate correlations along the spatial dimension (R^2). Considering jointly both statistics, the closest similarity occurs over grasslands with $R^2 = 0.67$; *rmse* = 0.67 μmol m^{-2} s^{-1} (GPP) and $R^2 = 0.46$; *rmse* = 0.97 μmol m^{-2} s^{-1} (NPP), along with evergreen needle-leaf forests (Taiga) with $R^2 = 0.51$; *rmse* = 0.94 μmol m^{-2} s^{-1} (GPP) and $R^2 = 0.46$; *rmse* = 0.7 μmol m^{-2} s^{-1} (NPP). Deciduous broad-leaf forests are also amongst the best correlated areas with $R^2 = 0.42$; *rmse* = 1.12 μmol m^{-2} s^{-1} (GPP) and $R^2 = 0.33$; *rmse*

= 0.94 μmol m^{-2} s^{-1} (NPP). The more spatially uncorrelated values ($R^2 = 0.01; 0.03$ for GPP and $R^2 = 0.01; 0.22$ for NPP) are found in shrublands and evergreen broad-leaf forests (tropical forests). For this classes, the *rmse* pointed to deviations of 0.32; 1.63 μmol m^{-2} s^{-1} (GPP) and 0.27; 1.0 μmol m^{-2} s^{-1} (NPP) respectively with regards MOD17A2H. The higher overestimations are found in managed crops with *rmse* = 3.15 μmol m^{-2} s^{-1} (GPP) and *rmse* = 3.21 μmol m^{-2} s^{-1} (NPP), leading to differences of 180%, with however stronger spatial correlations (R^2 up to 0.62).

Considering all the presented results, the conducted comparative analysis (Figs. 9–12) revealed that SCOPE-GPR-TCF products generally responded consistently with LPJ-GUESS and MOD17A2H. The degree of consistency is mostly driven by seasonality or spatial homogeneity. A special case is the tropical areas with soft seasonality and spatial complexity, leading to models presenting the sharpest inconsistencies.

4. Discussion

We introduced a workflow to monitor TCF dynamics globally using S3&5P data streams in combination with Bayesian GPR models. GPR
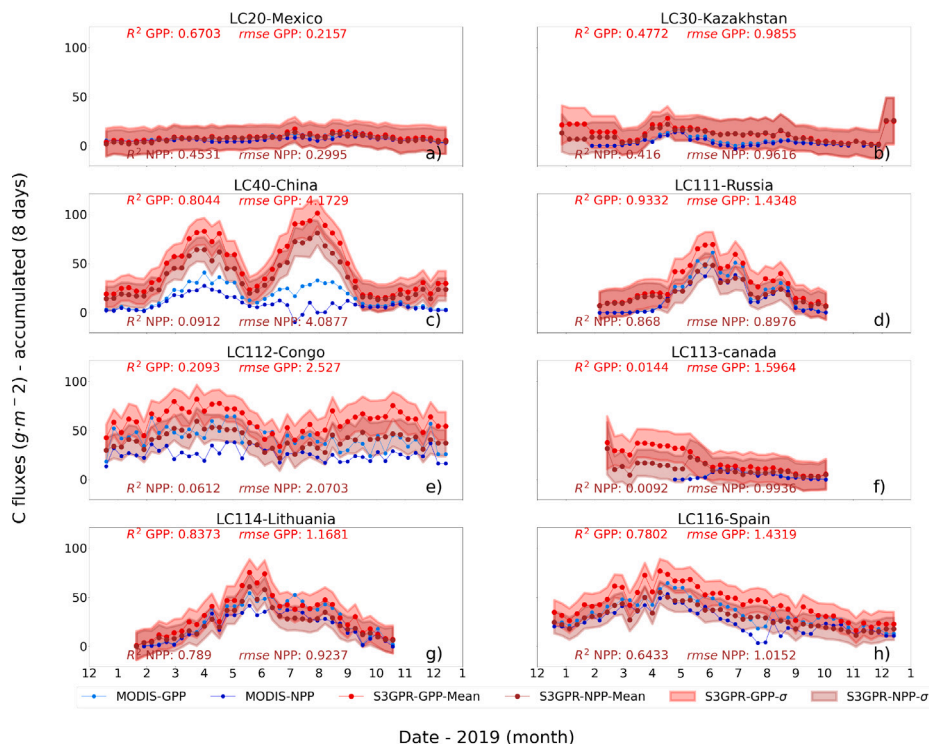
Fig. 11. Spatially-averaged time series of GPP and NPP over different sites as defined in Table 4, and cross-comparison against the MOD17A2H for the same areas. Temporal resolution of 8-days steps for the year 2019. From top-left to bottom-right (a) schrubland, (b) grassland, (c) managed cropland (mainly composed of wheat), (d) deciduous needle-leaf forest (e) evergreen broad-leaf forest, (f) evergreen needle-leaf forest, (g) deciduous broad-leaf forest, (h) evergreen Mediterranean forest mainly composed of cork oak.
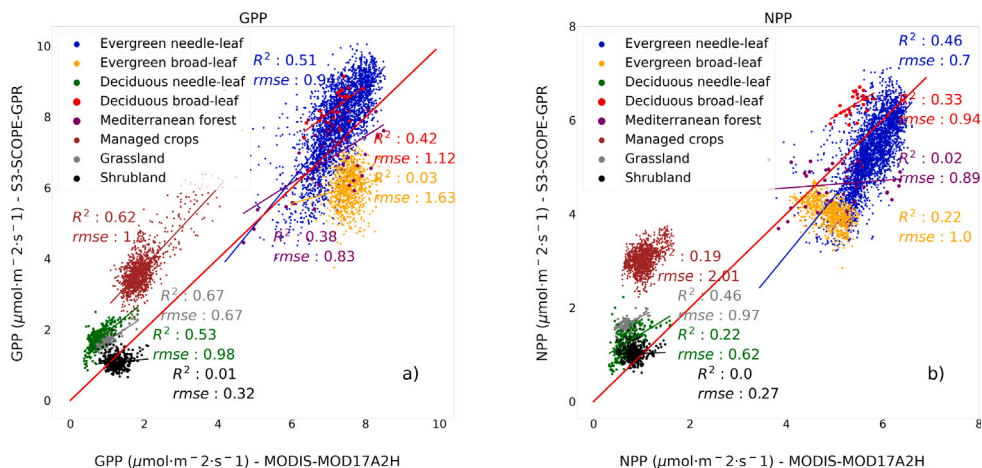

Fig. 12. Scatter plots showing spatial fit between SCOPE-GPR-TCF and MODIS-MOD17A2H for GPP (a) and NPP (b) grouped by land cover types (experimental areas). The analysis is applied to monthly temporal-composites (June 2019).

is an outstanding algorithm for retrieving terrestrial biophysical information along with uncertainties, still unexplored for inferring TCF. The generated GPP and NPP products have been evaluated at both local and global scales by comparing them against reference products: FLUXNET, LPJ-GUESS, and MOD17A2H. The internal consistency of the SCOPE-GPR-TCF products is spatially represented through the uncertainty layer (σ). We comment next on the performance of the models, stressing the role of the selected predictors followed by the identified sources of uncertainties.

4.1. Model predictors and their relative importance: SCOPE-GSA and GPR-rank

Based on the SCOPE-GSA result, the meteorological variable shortwave incident radiation was found to be the main input variable of GPP and NPP. SW is an essential variable in photosynthesis and was linked with the highest ST in the SCOPE-GSA, meaning that synergies were the strongest with the other inputs. The role of SW in SCOPE is also analysed in Yang et al. (2022). LAI, representing the total green vegetation surface, occupies the next position in the rank. LAI is

fundamental for describing vegetation canopy structure and therefore is especially important for modelling canopy functions (Reich, 2012; Brusa and Bunker, 2014; Xie et al., 2019; Parker, 2020).

The third position in the SCOPE-GSA ranking was occupied by V_{cmax}, which is neither directly measurable through satellite data nor used as a predictor in our models. We aimed to replace the information of V_{cmax} through SIF in the SCOPE-GPR-TCF models, given the strong correlation between these two variables (Camino et al., 2019).

The predictive importance of the eight input variables in the SCOPE-GPR-TCF models was subsequently assessed with the GPR-rank property (Fig. 4) and the analysis of estimates and σ layers (Fig. 7). LAI stood out as the main predictor, followed by SIF, FAPAR, and SW (with similar weights). FAPAR is an essential variable in LUE-based models (Monteith, 1972; Pei et al., 2022), and SIF has been directly linked with photosynthesis (Guan et al., 2016; Jonard et al., 2020; Han et al., 2022).

We searched for model optimization in terms of performance (e.g. highest R^2, lowest *rmse*) by initially testing multiple combinations of predictors (results not shown), consolidating in the set of the 8 presented variables scoring the highest. To demonstrate the synergy between SIF and the S3-OLCI vegetation traits (VT) for estimating TCF, alternative models removing predictors one by one were shown. As opposed to the reference SCOPE-GPR-TCF model based on the whole 8 predictors vector, the non-SIF model σ increased in specific areas. Over these surfaces, which often correspond to scarce vegetation, the predictors of the non-SIF model seem to fail. In this respect, Reyes-Muñoz et al. (2022) earlier reported that S3-derived VT products (e.g., LAI) suffered higher relative uncertainties over scarcely vegetated surfaces and bare soils. This limitation tends to be compensated by the information added by TROPOSIF in the version with the full set of predictors. The low values or absence of SIF over such surfaces help the model to make estimations more realistic of TCF.

4.2. Limitations and sources of uncertainties

Identifying limitations and sources of uncertainty is key to understanding the model's behaviour and guiding future improvements. The uncertainties (σ) provided by the SCOPE-GPR-TCF models revealed low to moderate levels with 10%–40% of estimates. Among the various factors that compromise the model's accuracy, the following five key aspects stand out:

• Application to global data streams:

We created a synthetic training database with SCOPE simulations to build the data-driven GPR hybrid models. To achieve this, the variables were drawn using defined sampling strategies with the overall aim of preparing a representative training dataset (De Grave et al., 2020). Reference works confirm the global representativeness of the main inputs employed. Asner et al. (2003) presented a global databases compilation of LAI campaigns for remote sensing applications with statistics in the ranges here employed (0–10 $m^2 m^{-2}$). Similar ranges typically appear in Fernandes et al. (2003, 2023) over forests in North America. LCC global reference data are nevertheless much more limited and the ranges were based on works with local/regional scope (De Grave et al., 2020; De Grave et al., 2021). The global representativity of the meteorological variables was insightfully verified from the ERA-5 data set (Hersbach et al., 2020). As for the variables maintained constant (e.g., atmospheric pressure, canopy height, leaf carotenoid content, leaf dry matter content), its distinctive role for predicting TCF was not fully addressed in this work. In particular, canopy height influences canopy structure, the scaling-up process from leaf to canopy, and the spatial and temporal variation in the environment (Wang et al., 2019). Leaf carotenoid is involved in energy transfer during photosynthesis, provides photoprotection and it has been used for tracking phenology of photosynthesis in evergreen forests (Wong et al., 2020). Nevertheless,

these biogeochemical processes are also captured to a larger extent by the set of considered input variables (e.g. LAI, FAPAR, SIF, SW), considered as key predictors in this work.

Moreover, one of the challenges faced by trained models is their performance on real-world data stream configurations (S3-based VT data alongside TROPOSIF and ERA5-LAND reanalysis data), which may not exhibit the same statistical properties as the data used during model training (Danner et al., 2021). While ML models are designed to learn patterns and make predictions based on the data they are trained on, they can encounter difficulties when applied to global data streams that diverge from their training set in terms of both the accuracy and uncertainty of the predictions and the statistical properties of the data. Moreover, the accuracy and uncertainty of the global predictors will directly influence the reliability of the simulation results, as discussed in the next section.

• Predictors accuracy:

Additionally, the final retrievals are affected by the accuracy of the predictors at lower levels (e.g., radiances, S3-derived VT retrievals, ERA5-LAND data). Any inaccuracies or uncertainties in these data streams propagate through the entire processing chain, potentially introducing noise and errors into the final TCF model results. Ensuring the highest possible precision in data acquisition and processing is crucial to obtaining reliable and meaningful information from satellite-based observations for various applications (Siddiqi et al., 2020), such as assessing GPP and NPP for terrestrial productivity monitoring.

Quantification of total uncertainty propagation based on the errors introduced by individual predictors can be assessed in various ways. For instance, in the case of non-linear functions, Taylor series expansion has been introduced (Gu et al., 2021). In our work, σ was used as a global indicator of SCOPE-GPR-TCF model uncertainty, implying that there is no prior information about uncertainty propagated by individual predictors. Nevertheless, the impact of adding or removing single predictors can serve as an indirect top-down approach to quantify the relative error added or removed by the targeted predictor in σ, as was shown through the comparison of maps generated by models excluding predictors.

• Non-linearity across temporal scales

To estimate TCF aggregated at 8-day time resolution, the SCOPE-GPR-TCF models were employed on predictor variables averaged over 8 days. This procedure was chosen instead of aggregating TCF from lower temporal scales (e.g., hours/day) due to (1) the lack of continuous hourly acquisitions (TROPOSIF) to obtain hourly TCF estimates and (2) homogenization with the temporal resolution of the S3-derived VT. While SCOPE-GPR-TCF is apt for capturing the non-linear relation between TCF and predictor variables for a specific point in time (see Fig. A.2; see Kim et al. (2021)), applying the SCOPE-GPR-TCF approach to predictors aggregated over time introduces a source of error. This is primarily due to the temporal resolution gap between the aggregated predictors and the intra-day variability that GPR is designed to capture. For exploring longer temporal scales, the SCOPE-GPR-TCF models here developed rely on 8-day means of predictors, implying that the intra-day patterns are concealed and might influence GPP estimates as a result of temporal aggregation. The expected error is higher when moving from hourly to daily aggregations compared to the transition from daily to 8-day steps due to the stronger intra-diurnal variability. An appendix (Figs. A.3 and A.4) demonstrates how this approximation could introduce bias in daily-scale retrievals. In general, overall matches between daily aggregated GPP partition estimates obtained by FLUXNET and SCOPE-GPR-GPP were close in absolute values, with bias varying between the different flux towers. However, tiny differences measured at a daily scale may imply substantial errors in annual terms (e.g. a difference of daily 1 $\mu mol \, m^{-2} \, s^{-1}$ annual extrapolated means a bias of 350 $gC \, m^{-2}$ or around 15% of total accumulated on temperate

forests). The experiment primarily addressed the impact of temporal aggregation, nevertheless, other factors such as predictor accuracy (e.g., LCC or SIF products), could contribute to the overall bias.

To quantify daily aggregated GPP values, the MOD17A2H product makes use of scalar variables calculated from daily aggregated minimum temperatures and mean vapour pressure deficits (affecting the light use efficiency), which also involves a gap due to temporal resolution. Within our approach, one way to consider intra-daily oscillations is to simulate TCF at different time steps and to train the models with the daily aggregated values. Real temporal profiles obtained from different locations and dates could be employed to accomplish such simulations; Alternatively, a simulator such as LPJ-GUESS or BEPS may integrate intra-daily values of TCF (Chen et al., 1999). However, the numerous combinations leading to similar aggregated values may also complicate the training data set size.

- Cloud-induced uncertainties

The accuracy of satellite-based remotely sensed data is highly susceptible to cloud cover, challenging global mapping of GPP in specific locations. These regions include latitudes between $\pm\,20°$, as visible in Fig. 6 over the Amazon, Congo Bay area, and the Malay Archipelago. Additionally, clouds present at shorter temporal spans (1–2 days) have a negative effect on generating temporal composite TCF products, due to fewer valid daily acquisitions. Furthermore, small clouds induce uncertainties by causing intra-pixel heterogeneity and shadowing vegetated land. These clouds introduce additional noise to remotely sensed signals and deteriorate the quality of the TCF product. As implemented by Kovács et al. (2023) the GEE-based Whittaker smoother (Whittaker, 1922) can be applied to temporally reconstruct cloud-free, continuous global vegetation products. Such gap-filling and smoothing can be considered as a follow-up step to improve overall TCF product consistency.

- Surface heterogeneity and spatial resolution:

The TCF models here developed relied on estimated S3-derived VT (LCC, LAI, FAPAR, FVC), which also contributed to the potential sources of uncertainty. The traits were obtained from L1B TOA radiance data collected by a hectometric resolution sensor: with 300 m ground sampling distance, OLCI images hinder their effective application at the local scale, especially in heterogeneous landscapes (e.g., Tang et al., 2021). Hence, the pixels encompass a variety of surface characteristics, including vegetation and soil, and also, they are affected by atmospheric conditions (Vermote et al., 1997). Conversely, the SCOPE simulations assume homogeneity within a pixel. As a consequence, the observed spectra deviate further from the training samples due to the increased heterogeneity in the pixel's composition (De Grave et al., 2020; Guanter et al., 2021). TROPOMI, with a GSD of 7 km × 3.5 km presents an even stronger constraint, especially when compared to tower scale products with their defined footprint. In fact, we observed a poorer accuracy of the models validated with some flux towers located in croplands (see also Fig. A.6). Upon detailed analysis at these sites, it was observed that land cover comprises a diversity of parcels within a relatively short distance of some hundred meters. This resulted in the signal received by the satellites becoming mixed and, consequently, deviating from the tower footprint. Surface heterogeneity can also explain the weaker correlations found between SCOPE-GPR-TCF and MOD17A2H for the different land cover analysed, especially marked for evergreen broad-leaf leaf forests, entailing a strong spatial diversity. As a rule, the level of surface heterogeneity depends on the analysis scale and the sensor spatial resolution, with an error magnitude governed by these two factors (Xie et al., 2022).

4.3. Validation of SCOPE-GPR-TCF at flux tower sites

The cross-comparison of the GPP temporal trends against the flux tower (FLUXNET) partition estimates represented the in-situ validation. Beyond this comparison, it was not possible to validate the NPP variable against in-situ data since the FLUXNET products derived from NEE do not quantify specifically vegetation respiration. The temporal analysis of GPP revealed that the annual phenology was well reconstructed by SCOPE-GPR-GPP, except for a few sites. Validation with R^2 below 0.4 was not frequent in most cases, except for EBF. The predictions were mostly in the observed ranges, except for the case of EBF linked with values of *rmse* above 5 $\mu\mathrm{mol\,m^{-2}\,s^{-1}}$. As previously discussed, factors such as surface heterogeneity and a lack of seasonality could explain the poorest retrievals. Cross-comparison over heterogeneous surfaces may additionally lead to varying performances in the cases that the tower data fall over the centre or towards the edge of the input pixels (i.e., TROPOSIF, S3-derived VT), a question addressed by Li and Xiao (2022). Their work studied the relationship between TROPOSIF and GPP as a function of the distance to the centre of SIF soundings and the grid size. Typically, removal of tower data located on heterogeneous surfaces (Doughty et al., 2023) or at a maximal distance from the sounding points (Balde et al., 2023) are employed. Nevertheless, here we chose to include the full set of available towers, given that the available data are limited to the year 2019, where the input products were merged to study their synergy at a global scale. Uncertainties of the flux towers observations are an additional factor that may contribute to observed differences (Joiner et al., 2018). Furthermore, while generally high convergence was found between the SCOPE-GPR-GPP and FLUXNET GPP partition estimates, factors such as the temporal aggregation can also impact the statistics R^2 and *rmse*. For instance, Pierrat et al. (2022) and Doughty et al. (2023) reported superior R^2 and *rmse* values when applying cross-comparisons against eddy covariance towers at a monthly temporal resolution (compared with the 8-days analysis applied in our case). Balde et al. (2023) also presented a method based on random forest to estimate GPP from TROPOSIF and MODIS reflectances, reaching higher validation performances against flux towers observations. Nevertheless, the site-level scope of their models is restricted to conditions found on selected flux towers in Europe. In contrast, the application of SCOPE-GPR-TCF is aimed at global scale extrapolation, validated with independent observations (GPP) at different points of the globe. However, a full validation of the NPP product against in-situ data remains pending. In this regard, Endsley et al. (2023), who presented continuity of the global MODIS TCF products in the VIIRS era, validated their NPP product over 1600 sites using an inventory of data sets collected by the Oak Ridge National Laboratory (ORNL) Distributed Active Archive Center, (for example Scurlock et al. (2003)). Alternatively, Wang et al. (2021a) presented another set of GPP/NPP products based on LUE parameterization validated against data from the BigFoot initiative (https://daac.ornl.gov/cgi-bin/dataset_lister.pl?p=1). Although the temporal ranges of these validation data sets do not match the dates for the presented SCOPE-GPR-TCF products, the developed NPP products by Endsley et al. (2023) and Wang et al. (2021a) could alternatively serve for benchmarking.

4.4. Global performance of SCOPE-GPR-TCF models in relation to reference products

Benchmarking the SCOPE-GPR-TCF products against established TCF products becomes crucial to evaluating their accuracy and consistency. In this context, the LPJ-GUESS L3 and MOD17A2H products were used to cross-compare the consistency of the SCOPE-GPR-TCF products. Generally, our hybrid models proved to behave consistently with the reference products. At the global scale, the estimations of TCF move around ranges comparable to those of LPJ-GUESS and MOD17A2H. The results of GPP are more tight-fitting to MOD17A2H,

relying on satellite images with a more similar spatial resolution than the one provided by LPJ-GUESS. GPP estimated by SCOPE-GPR-TCF models matched more closely to MOD17A2H than the NPP product; the poorer matching of NPP can be attributed to the fact that it is a more complex variable depending additionally on maintenance respiration. SCOPE-GPR-TCF seasonality was well cross-correlated with LPJ-GUESS and MOD17A2H at mid-high latitudes. Discrepant phenological patterns were found mainly over evergreen tropical forests. In this latitude, the climate is more steady, and phenology, which is highly dependent on climatic variability, is therefore not clearly marked. These results coincide with Ardö (2015), which also observed similar temporal mismatches over the same biomes when comparing GPP estimations from satellite data and process-based dynamic global vegetation models (DGVMs). Conversely, according to Prentice and Cowling (2013), most DGVMs use a simple growing degree day index to predict the growing season and are therefore more accurate for high latitude climates. In subtropical regions (Southern hemisphere), the negative correlations between LPJ-GUESS and SCOPE-GPR-TCF can be explained due to the straightforward response of grass and shrubs to precipitation (Papagiannopoulou et al., 2017), a variable that is not included in SCOPE-GPR-TCF. The same mismatch was also found in LPJ-GUESS and MOD17A2H cross-correlation maps (see Fig. A.1). When observing the time series intra-annual cross-correlation with MOD17A2H over defined land cover types (see Fig. 11), generally we found a good match, except for the discussed tropical areas, and the wheat and maize croplands in Henan (Li et al., 2023), where a substantial overestimation appeared. In any case, the phenological pattern correlated well and corresponded to calendar observations available from https://ipad.fas.usda.gov/ogamaps/cropcalendar.aspx IPAD (International Production Assessment Division) of the USA Department of Agriculture (accessed on 12Th March 2023). Overall, the global distribution of SCOPE-GPR-TCF aligns with the results obtained by other authors in terms of spatial variability and total annual quantities (Doughty et al., 2023; Wang et al., 2021b; Li and Xiao, 2019).

4.5. Advantages and limitations of the hybrid GPR-based models

As opposed to established TCF products relying on empirical LUE models, for instance, the MOD17A2H product (Running et al., 2015), our models offer the distinct advantage of being relatively efficient in generating global TCF products at moderately spatial and temporal resolutions. Based on the premise that representative training datasets are generated by the employed RTM, such as SCOPE, GPR hybrid models have the advantage of being independent of field measurements, which are typically needed in pure LUE approaches.

Furthermore, process-based models such as LPJ-GUESS or OR-CHIDEE provide operational predictions of global surface carbon fluxes typically at spatial resolutions from 0.5° and beyond. In contrast, our method provides a computationally efficient method able to map at higher spatial resolutions (i.e., 300 m) using satellite data. In addition, the hybrid approach allows predictions without dealing with complex parameterizations, as also observed by Zhang et al. (2016), although this depends on the complexity of the involved process-based model.

As the fundamental algorithm of the proposed method, GPR offers a notable advantage over alternative ML approaches by providing associated uncertainties. This capability allows for robust model application to new and varied datasets, enabling deeper exploration of the model's behaviour and performance across ranging environmental conditions. Jung et al. (2020) also highlighted the potential of this feature to improve FLUXCOM, an initiative to provide global products of TCF (GPP, NEE and ecosystem respiration) through satellite data and several ML regression toolboxes http://www.fluxcom.org/. Moreover, GPR proves to be cost-effective when dealing with small sample sizes (Camps-Valls et al., 2018). The kernels allow for defining the Gaussian functions over the space capturing complex non-linear patterns without overfitting. The definition of such functions takes

place typically with sample sizes much smaller than other algorithms such as neural networks.

On the downside, GPR implementation leans on multidimensional array operations, which can lead to RAM limitations when the models are excessively heavy (see also Pipia et al. (2021)). Consequently, as lightweight models are required for seamless global processing, they may perform less accurately at specific locations, since they were not trained for the local conditions (e.g. the BE-Lon site). A similar limitation was found by Beer et al. (2010) when applying data-adaptive ML to extrapolate models to completely different conditions. This points again towards the necessity of providing the most representative training datasets, which for instance can be achieved by intelligent sampling strategies, such as active learning (e.g., Verrelst et al., 2016a; Berger et al., 2021). It could further be considered to design retrieval models customized for particular conditions, a strategy that may involve employing techniques such as stratification. Other approaches to extrapolate to distinct conditions consider the usage of ensembles with in situ data (Jung et al., 2020) or a combination of simulated and experimental data (Camps-Valls et al., 2018).

4.6. Global mapping in GEE

GEE has demonstrated its versatility as a cloud computing platform for rapidly accessing planetary-scale satellite products. For the presented workflow, the retrieval of GPP and NPP maps was greatly aided by the available preprocessed multi-petabyte dataset library containing useful products, such as ERA5-Land data or the S3 OLCI catalogue. Amongst others, satellite GPP products are available on the GEE platform, for example, MOD17A2H, which allows for cross-comparison against our retrieved products (Running et al., 2015; Robinson et al., 2018). Furthermore, GEE provides a large set of built-in functions for processing and analysing data, making standardized tasks (e.g., arithmetic operations, statistics) simple, counting on massive computation power (Gorelick et al., 2017). However, these built-in functions are closed, and the implementation of new procedures beyond the scope of the available tools requires significant effort (Gomes et al., 2020).

We had to overcome the following challenges when applying our method in GEE: (1) The large amount of memory demanded by the GPR algorithm. Despite counting on massive resources for processing through connected CPUs, GEE provides a limited quota for RAM usage (Gorelick et al., 2017), thus the referred lightweight model strategy needed to be carried out even using GEE. (2) The integration of external data in batches on the platform. To involve data that is not available by default, we have used the Python Command Line Interface (CLI) *geeup* (Roy, 2023) to upload large datasets of external data, such as TROPOSIF. The capability to run GEE with Python codes and libraries offers powerful extensions to the already-available tools and solutions the platform offers.

4.7. Future work

The Copernicus program introduces new-generation satellites with cutting-edge instruments demanding innovative approaches to extract their captured information (Berger et al., 2012), unlike the data from MODIS, which has been extensively exploited and has outlived its design life. The results presented here pave the path towards novel strategies to improve inferring TCF products entirely from Copernicus and ESA data. The flexibility of the hybrid strategy enables us to readily generate retrievals using new data sources, anticipating ESA's upcoming FLEX mission. Combining SIF measurements from FLORIS (FLEX) with vegetation structure, pigments, and land surface temperature products from OLCI, and SLSTR (S3) in the FLEX-S3 tandem mission, will allow us to explore the impact of climate variability, land use changes, and biotic and abiotic environmental stressors on TCF dynamics (Van Wittenberghe et al., 2021). This integrated approach

offers exciting prospects for advancing our understanding of TCF and its interactions with various environmental factors.

Finally, the application of GPR to achieve data-driven models trained directly with field-measured data presents an alternative to the here presented hybrid workflow. Along this line, the flux tower measurements used to validate the global SCOPE-GPR-TCF models with information on the ground, also open new paths for the global scaling of carbon fluxes. For instance, Zeng et al. (2020) and Jung et al. (2020) explored the use of multiple ML algorithms to study GPP (and NEE) trained from eddy covariance data. The approach involves the usage of real data streams, presumably avoiding a source of uncertainty due to the usage of a synthetic training dataset to represent real environments, although it also involves the challenge of selecting enough samples to generalize global conditions. The field-measured data-driven approach further allows the prediction of other targeted variables as available from the flux tower measurements, such as NEE or ecosystem respiration (Zeng et al., 2020; Jung et al., 2020). Future work investigating this direction will be fundamental to exploring further improvements in data-driven methods, particularly in relation to the presented hybrid workflow and in view of the upcoming FLEX era.

5. Conclusions

With the anticipation of open-access global data streams of new-generation satellite products, along with enhanced modelling approaches and cloud computing facilities, prospects are emerging for routinely monitoring terrestrial carbon fluxes at customized scales. Here we presented a novel hybrid processing workflow, leveraging the coupling of SCOPE simulations with GPR models, and harnessing the synergistic integration of Sentinel-3 and Sentinel-5P data with the ERA5 climate reanalysis models and derived vegetation products. The SCOPE-GPR-TCF models demonstrated remarkable potential for global spatiotemporal vegetation TCF mapping and emphasized the critical role of LAI, FAPAR, and SIF as key variables in building robust models. Furthermore, the consistent intra-annually cross-correlation of estimated TCF products observed across multiple biomes and land cover types, against FLUXNET (GPP), LPJ-GUESS (GPP) and MOD17A2H (GPP and NPP) products, confirmed the reliability and applicability of our workflow. The efficiency and computational power of GEE played a crucial role in the processing and analysis of the vast amounts of satellite data involved in this study. GEE's capabilities significantly expedited the map generation and temporal analysis tasks, making it an invaluable tool for large-scale investigations and global mapping of TCF products.

The main contribution of our work is as follows:

- Global processing of TCF products can be addressed at an efficient cost through the implementation of GPR in a cloud environment (GEE). The synergy of ML with cloud computing presents an accessible and open option for the scientific community, enabling the execution of models at any desired time window and focusing on specific regions of interest.
- The GPR outputs offer a straightforward approach to address research on uncertainty factors and predictors' significance. By analysing the σ values, insights can be attained into the uncertainties associated with models, and the relative importance of different variables in the prediction process can be identified. LAI, FAPAR, and SIF turned out to be key driving predictors.
- Instantaneous mapping was demonstrated with maximum global values of 25 μmol m^{-2} s^{-1} (GPP) and 16 μmol m^{-2} s^{-1} (NPP). Annual aggregated values (2019) reached maximums of 4000 gC m^{-2} y^{-1} (GPP) and 3200 gC m^{-2} y^{-1} (NPP). Uncertainty layers reflected low to moderate deviations (10%–40%) around the globe. Furthermore, spatiotemporal patterns were cross-compared against FLUXNET, LPJ-GUESS, and MOD17A2H data streams, presenting consistent correlations.

- The implemented workflow facilitates the exploration of data synergies among multiple satellite products, significantly enhancing the capacity for scalable spatiotemporal monitoring of TCF.

In conclusion, the presented workflow provides a cloud-computing-based scalable approach to map vegetation productivity across local to global scales efficiently. We anticipate applying this workflow to the S3-FLEX tandem mission when FLEX is launched and starts transmitting data. Eventually, the derived vegetation and TCF products at a spatial resolution of 300 m will enhance our understanding of TCF dynamics and diverse ecological processes, empowering us to tackle challenges related to global climate change more effectively.

CRediT authorship contribution statement

Pablo Reyes-Muñoz: Writing – review & editing, Writing – original draft, Visualization, Validation, Software, Resources, Methodology, Investigation, Formal analysis, Conceptualization. **Dávid D.Kovács:** Writing – review & editing, Writing – original draft, Visualization, Resources, Formal analysis. **Katja Berger:** Writing – review & editing, Supervision, Formal analysis, Conceptualization. **Luca Pipia:** Supervision, Software, Methodology. **Santiago Belda:** Supervision, Methodology. **Juan Pablo Rivera-Caicedo:** Software. **Jochem Verrelst:** Writing – review & editing, Supervision, Methodology, Investigation, Funding acquisition, Formal analysis, Conceptualization.

Declaration of competing interest

The authors declare that they have no known competing financial interests or personal relationships that could have appeared to influence the work reported in this paper.

Data availability

The code is shared in an open Github repository. The link to the repository is shown in the attached draft.

Acknowledgements

Appendix A

See Figs. A.1–A.6.

Appendix B. Supplementary material

The code developed to map TCF, and open for the community, is available in the repository https://github.com/psreyes/TCF_mapping (accessed on 3 September 2023)
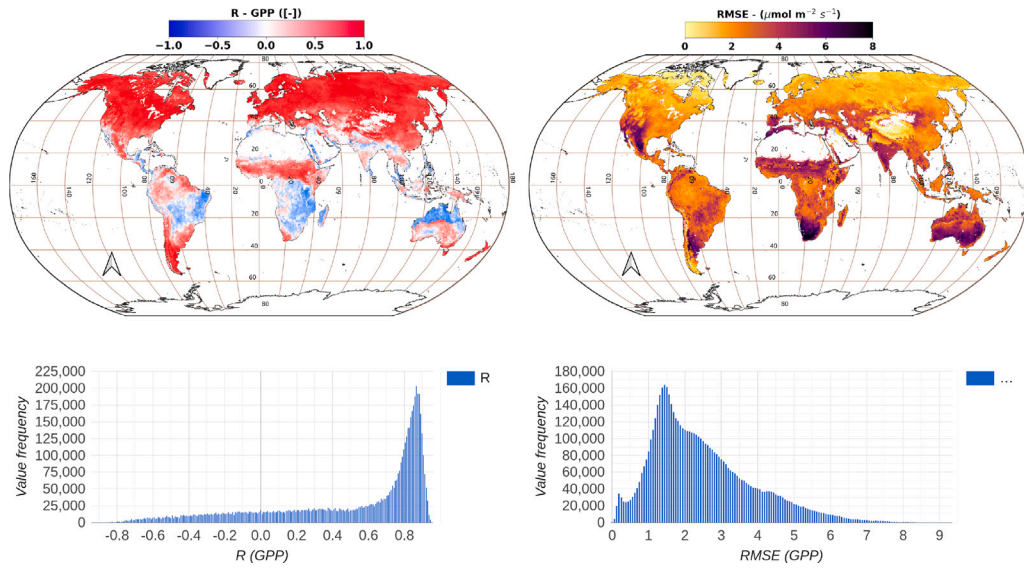
Fig. A.1. Intra-annual correlation (year 2019) between MODIS and LPJ-GUESS (GPP). Both datasets consisted of 8-days temporal composited global products.
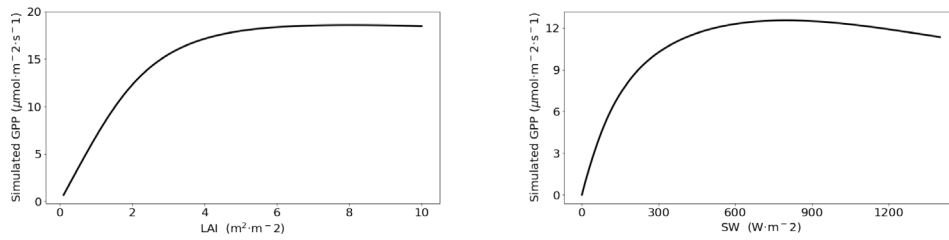

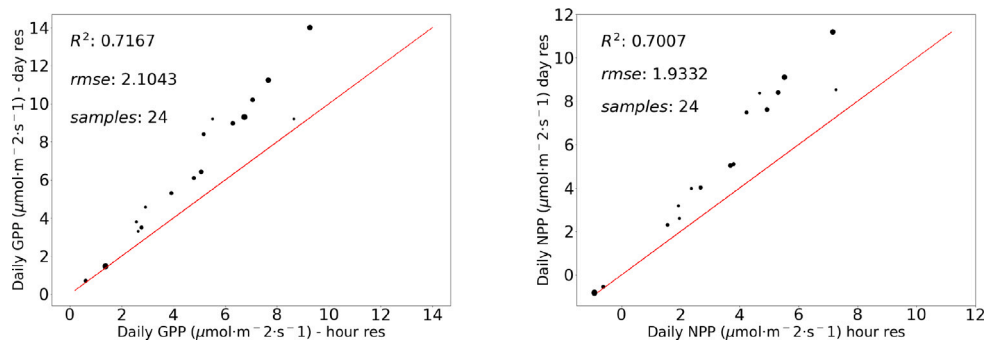**Fig. A.2.** GPP Non-linear response profile to the mean predictors: SW (a) and LAI (b).

Fig. A.3. GPP (a) and NPP (b) non-linear profile across temporal resolution scales (hourly vs daily). The test was performed by simulating daily GPP and NPP both at half-hour and daily resolution from meteorological conditions observed at flux towers. For the test, only SW, TA and EA were ranged, keeping other variables constant. LAI in-situ measurements were also employed. The size of the points are proportional to the measured LAI.
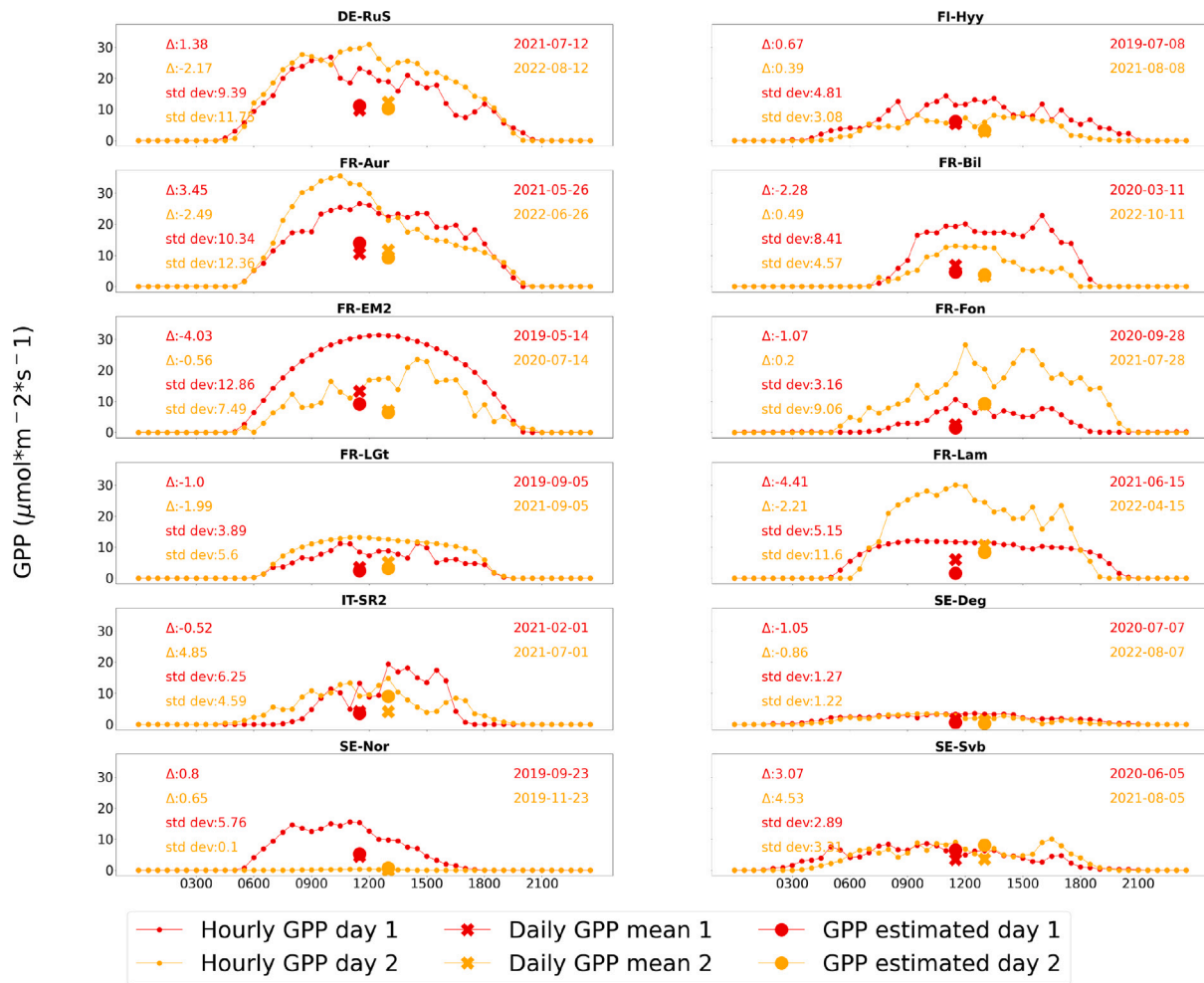
Fig. A.4. Intra-daily profiles of GPP partition estimates obtained from eddy-covariance measurements at different tower sites for inter-comparison with SCOPE-GPR-TCF daily-aggregated values. Eddy-covariance hourly observations were averaged over 24 h and then compared with SCOPE-GPR-TCF retrievals at a daily resolution.
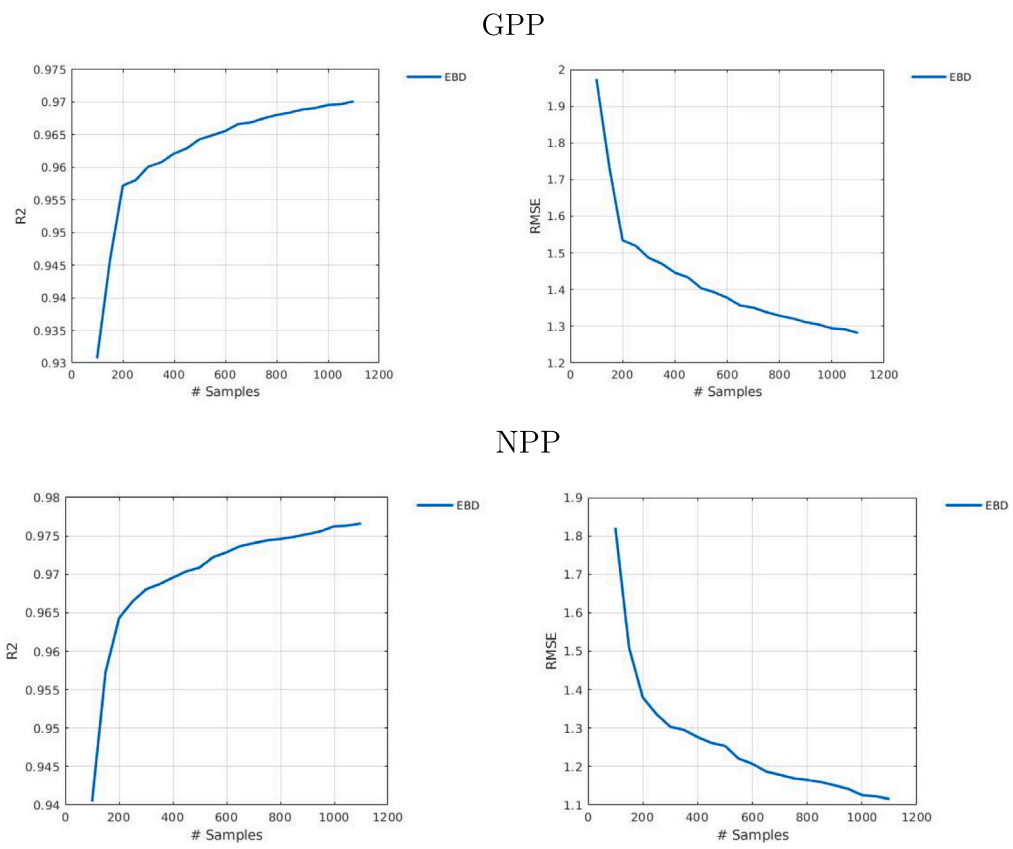
GPP

NPP

Fig. A.5. Performance as a function of sample size for training models of GPP (first row) and NPP (second row).
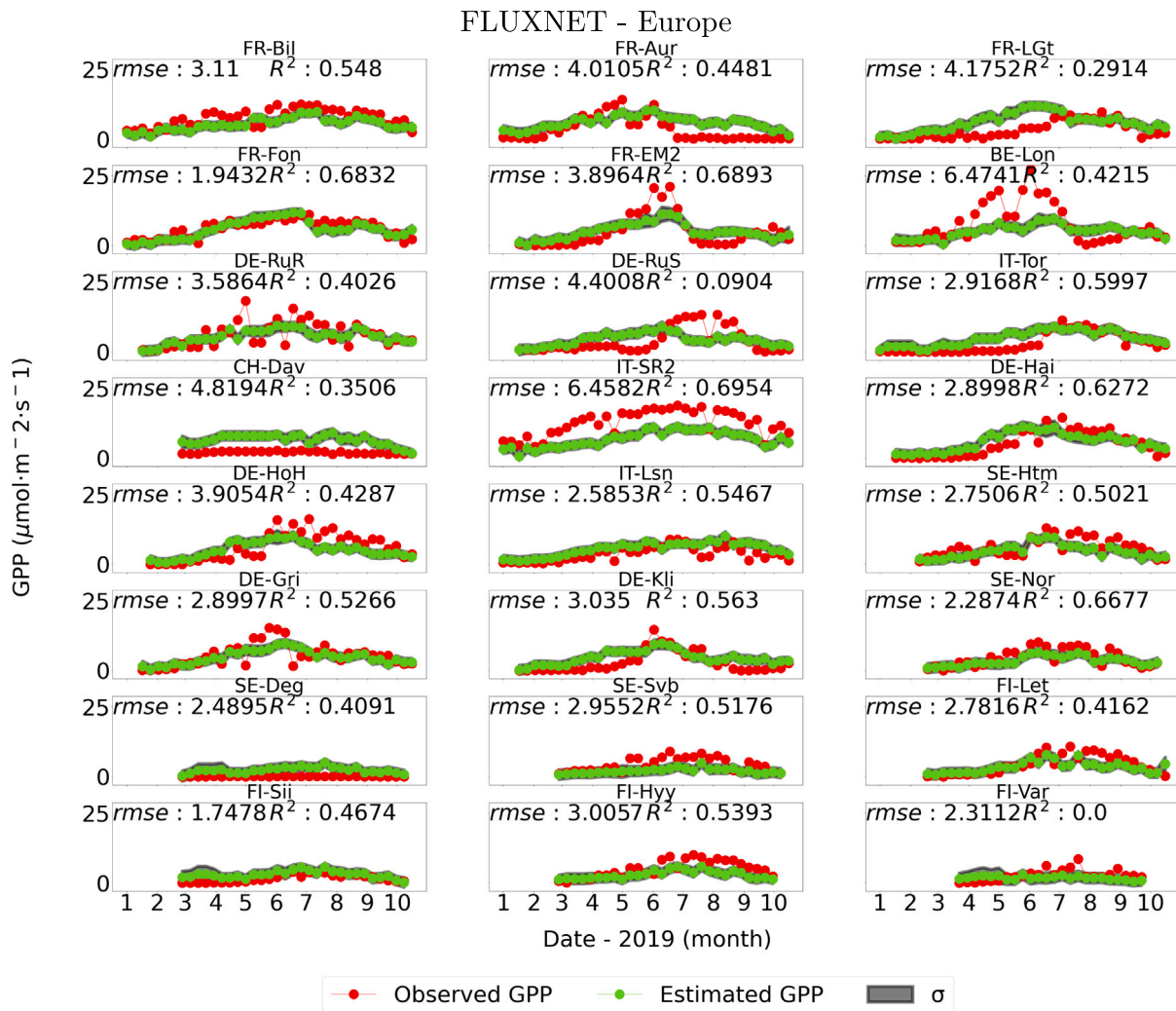
Fig. A.6. Intercomparison of GPP estimations at 113 flux tower sites over Europe and America.
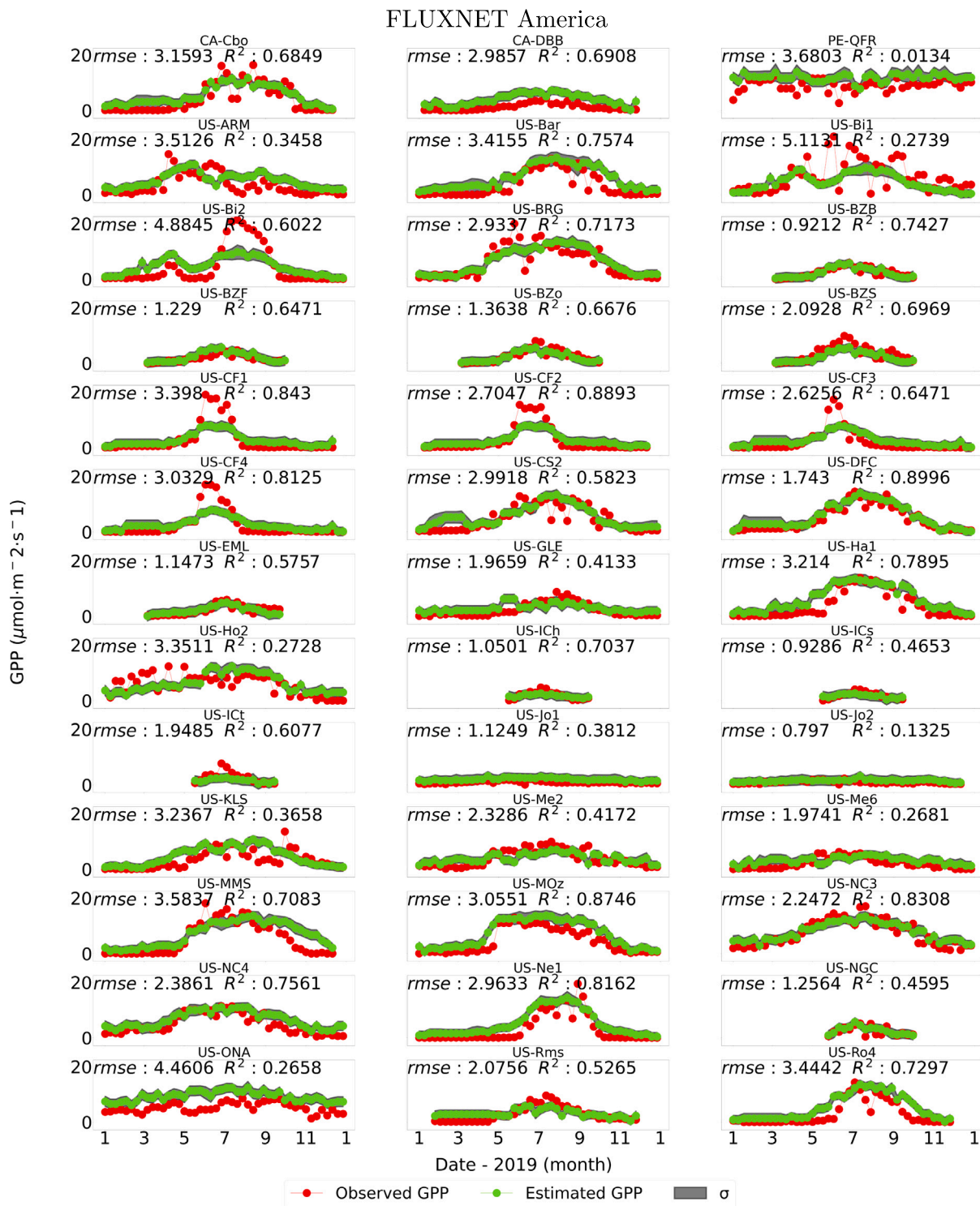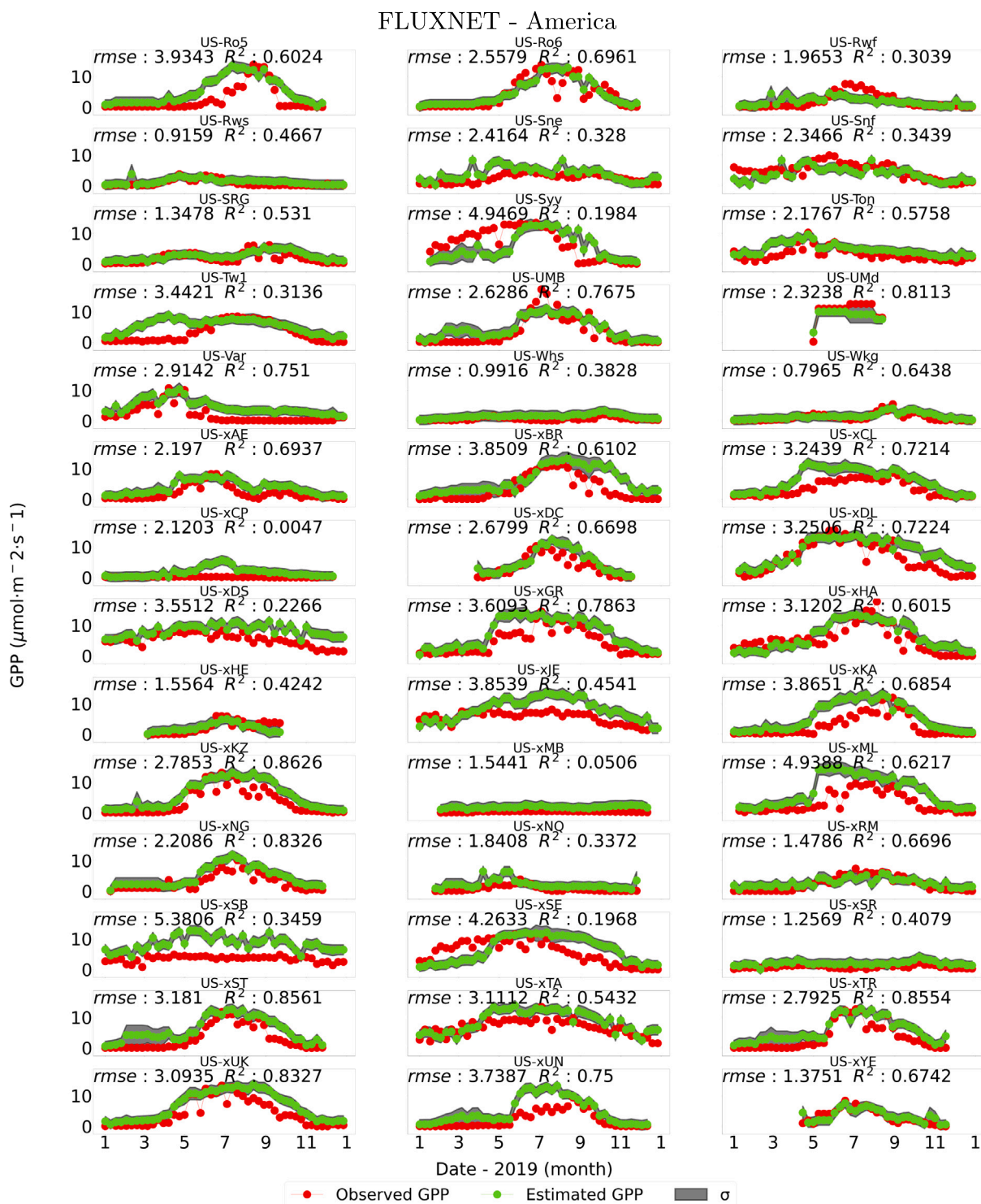
Fig. A.6. (*continued*).

Fig. A.6. (*continued*).

References

Ardö, J., 2015. Comparison between remote sensing and a dynamic vegetation model for estimating terrestrial primary production of Africa. Carbon Balance Manage. 10 (1), 8. http://dx.doi.org/10.1186/s13021-015-0018-5.

Asner, G., Scurlock, J., Hicke, J., 2003. Global synthesis of leaf area index observations: implications for ecological and remote sensing studies: Global leaf area index. Global Ecol. Biogeogr. 12, 191–205. http://dx.doi.org/10.1046/j.1466-822X.2003.00026.x.

Ayala Izurieta, J.E., Jara Santillán, C.A., Márquez, C.O., García, V.J., et al., 2022. Improving the remote estimation of soil organic carbon in complex ecosystems with Sentinel-2 and GIS using Gaussian processes regression. Plant Soil 479 (1), 159–183. http://dx.doi.org/10.1007/s11104-022-05506-1.

Balde, H., Hmimina, G., Goulas, Y., Latouche, G., Soudani, K., 2023. Synergy between TROPOMI sun-induced chlorophyll fluorescence and MODIS spectral reflectance for understanding the dynamics of gross primary productivity at Integrated Carbon Observatory System (ICOS) ecosystem flux sites. Biogeosciences 20 (7), 1473–1490. http://dx.doi.org/10.5194/bg-20-1473-2023.

Baldocchi, D., Falge, E., Gu, L., Olson, R., et al., 2001. FLUXNET: A new tool to study the temporal and spatial variability of ecosystem-scale carbon dioxide, water vapor, and energy flux densities. Bull. Am. Meteorol. Soc. 82 (11), 2415–2434. http://dx.doi.org/10.1175/1520-0477(2001)082<2415:FANTTS>2.3.CO;2.

Balzarolo, M., Anderson, K., Nichol, C., Rossini, M., et al., 2011. Ground-based optical measurements at European flux sites: A review of methods, instruments and current controversies. Sensors 11 (8), 7954–7981. http://dx.doi.org/10.3390/s11087954.

Beer, C., Reichstein, M., Tomelleri, E., Ciais, P., et al., 2010. Terrestrial gross carbon dioxide uptake: Global distribution and covariation with climate. Science 329 (5993), 834–838. http://dx.doi.org/10.1126/science.1184984.

Berger, K., Atzberger, C., Danner, M., D'Urso, G., Mauser, W., Vuolo, F., Hank, T., 2018. Evaluation of the PROSAIL model capabilities for future hyperspectral model environments: A review study. Remote Sens. 10 (1), 85. http://dx.doi.org/10.3390/rs10010085.

Berger, K., Machwitz, M., Kycko, M., Kefauver, S.C., et al., 2022. Multi-sensor spectral synergies for crop stress detection and monitoring in the optical domain: A review. Remote Sens. Environ. 280, 113198. http://dx.doi.org/10.1016/j.rse.2022.113198.

Berger, M., Moreno, J., Johannessen, J.A., Levelt, P.F., Hanssen, R.F., 2012. Esa's sentinel missions in support of Earth system science. Remote Sens. Environ. 120, 84–90. http://dx.doi.org/10.1016/j.rse.2011.07.023, The Sentinel Missions - New Opportunities for Science.

Berger, K., Rivera Caicedo, J.P., Martino, L., Wocher, M., Hank, T., Verrelst, J., 2021. A Survey of Active Learning for Quantifying Vegetation Traits from Terrestrial Earth Observation Data. Remote Sens. 13 (2), 287. http://dx.doi.org/10.3390/rs13020287.

Bracho, R., Starr, G., Gholz, H., Martin, T., Cropper, W., Loescher, H., 2012. Controls on carbon dynamics by ecosystem structure and climate for southeastern U.S. slash pine plantations. Ecol. Monograph 82, 101–128. http://dx.doi.org/10.2307/23206687.

Brusa, A., Bunker, D., 2014. Increasing the precision of canopy closure estimates from hemispherical photography: Blue channel analysis and under-exposure. Agricult. Forest Meteorol. s 195–196, 102–107. http://dx.doi.org/10.1016/j.agrformet.2014.05.001.

Buchhorn, M., Lesiv, M., Tsendbazar, N.E., Herold, M., Bertels, L., Smets, B., 2020. Copernicus global land cover layers—Collection 2. Remote Sens. 12 (6), http://dx.doi.org/10.3390/rs12061044.

Caemmerer, S., 2000. Biochemical Models of Leaf Photosynthesis. http://dx.doi.org/10.1071/9780643103405.

Camino, C., Gonzalez-Dugo, V., Hernandez, P., Zarco-Tejada, P.J., 2019. Radiative transfer Vcmax estimation from hyperspectral imagery and SIF retrievals to assess photosynthetic performance in rainfed and irrigated plant phenotyping trials. Remote Sens. Environ. 231, 111186. http://dx.doi.org/10.1016/j.rse.2019.05.005.

Camps-Valls, G., Martino, L., Svendsen, D., Campos-Taberner, M., Muñoz, J., et al., 2018. Physics-aware Gaussian processes in remote sensing. Appl. Soft Comput. 68, http://dx.doi.org/10.1016/j.asoc.2018.03.021.

Camps-Valls, G., Verrelst, J., Munoz-Mari, J., Laparra, V., Mateo-Jimenez, F., Gomez-Dans, J., 2016. A survey on Gaussian processes for Earth-observation data analysis: A comprehensive investigation. IEEE Geosci. Remote Sens. Mag. 4 (2), 58–78. http://dx.doi.org/10.1109/MGRS.2015.2510084.

Chen, J.M., Liu, J., Cihlar, J., Goulden, M.L., 1999. Daily canopy photosynthesis model through temporal and spatial scaling for remote sensing applications. Ecol. Model. 124 (2–3), 99–119. http://dx.doi.org/10.1016/S0304-3800(99)00156-8.

Chen, A., Ricciuto, D., Mao, J., Wang, J., Lu, D., Meng, F., 2023. Improving E3SM land model photosynthesis parameterization via satellite SIF, machine learning, and surrogate modeling. J. Adv. Modelling Earth Syst. 15 (4), e2022MS003135. http://dx.doi.org/10.1029/2022MS003135, e2022MS003135 2022MS003135.

Crisp, D., Pollock, H.R., Rosenberg, R., Chapsky, L., et al., 2017. The on-orbit performance of the orbiting carbon observatory-2 (OCO-2) instrument and its radiometrically calibrated products. Atmos. Meas. Tech. 10 (1), 59–81. http://dx.doi.org/10.5194/amt-10-59-2017.

Croft, H., Chen, J.M., Luo, X., Bartlett, P., Chen, B., Staebler, R.M., 2017. Leaf chlorophyll content as a proxy for leaf photosynthetic capacity. Global Change Biol. 23 (9), 3513–3524. http://dx.doi.org/10.1111/gcb.13599, arXiv:27976452.

Danner, M., Berger, K., Wocher, M., Mauser, W., Hank, T., 2021. Efficient RTM-based training of machine learning regression algorithms to quantify biophysical & biochemical traits of agricultural crops. ISPRS J. Photogramm. 173, 278–296. http://dx.doi.org/10.1016/j.isprsjprs.2021.01.017.

De Grave, C., Pipia, L., Siegmann, B., Morcillo-Pallarés, P., Rivera Caicedo, J., Moreno, J., Verrelst, J., 2021. Retrieving and validating leaf and canopy chlorophyll content at moderate resolution: A multiscale analysis with the sentinel-3 OLCI sensor. Remote Sens. 13, 1419. http://dx.doi.org/10.3390/rs13081419.

De Grave, C., Verrelst, J., Morcillo-Pallarés, P., Pipia, L., et al., 2020. Quantifying vegetation biophysical variables from the sentinel-3/FLEX tandem mission: Evaluation of the synergy of OLCI and FLORIS data sources. Remote Sens. Environ. 251, 112101. http://dx.doi.org/10.1016/j.rse.2020.112101.

Delwiche, K.B., Knox, S.H., Malhotra, A., Fluet-Chouinard, E., et al., 2021. FLUXNET-CH4: a global, multi-ecosystem dataset and analysis of methane seasonality from freshwater wetlands. Earth Syst. Sci. Data 13 (7), 3607–3689. http://dx.doi.org/10.5194/essd-13-3607-2021.

Dong, J., Xiao, X., Wagle, P., Zhang, G., et al., 2015. Comparison of four EVI-based models for estimating gross primary production of maize and soybean croplands and tallgrass prairie under severe drought. Remote Sens. Environ. 162, 154–168. http://dx.doi.org/10.1016/j.rse.2015.02.022.

Dou, X., Yang, Y., 2018. Estimating forest carbon fluxes using four different data-driven techniques based on long-term eddy covariance measurements: Model comparison and evaluation. Sci. Total Environ. 627, 78–94. http://dx.doi.org/10.1016/j.scitotenv.2018.01.202.

Doughty, R., Wang, Y., Johnson, J., Parazoo, N., et al., 2023. A novel data-driven global model of photosynthesis using solar-induced chlorophyll fluorescence. http://dx.doi.org/10.22541/essoar.168167172.20799710/v1.

Drusch, M., Moreno, J., Del Bello, U., Franco, R., et al., 2017. The fluorescence EXplorer mission concept—ESA's Earth explorer 8. IEEE Trans. Geosci. Remote Sens. 55 (3), 1273–1284. http://dx.doi.org/10.1109/TGRS.2016.2621820.

Endsley, K.A., Zhao, M., Kimball, J.S., Devadiga, S., 2023. Continuity of global MODIS terrestrial primary productivity estimates in the VIIRS era using model-data fusion. J. Geophys. Res. Biogeosciences 128 (9), e2023JG007457. http://dx.doi.org/10.1029/2023JG007457, e2023JG007457 2023JG007457.

Estévez, J., Salinero-Delgado, M., Berger, K., Pipia, L., et al., 2022. Gaussian processes retrieval of crop traits in Google Earth Engine based on Sentinel-2 top-of-atmosphere data 273. (ISSN: 0034-4257) 112958. http://dx.doi.org/10.1016/j.rse.2022.112958.

Farquhar, G.D., von Caemmerer, S., Berry, J.A., 1980. A biochemical model of photosynthetic CO2 assimilation in leaves of C3 species. Planta 149 (1), 78–90. http://dx.doi.org/10.1007/BF00386231.

Fernandes, R., Brown, L., Canisius, F., Dash, J., et al., 2023. Validation of Simplified Level 2 Prototype Processor Sentinel-2 fraction of canopy cover, fraction of absorbed photosynthetically active radiation and leaf area index products over North American forests. Remote Sens. Environ. 293, 113600. http://dx.doi.org/10.1016/j.rse.2023.113600.

Fernandes, R., Butson, C., Leblanc, S., Latifovic, R., 2003. Landsat-5 TM and Landsat-7 ETM+ based accuracy assessment of leaf area index products for Canada derived from SPOT-4 VEGETATION data. Can. J. Remote Sens. 29 (2), 241–258. http://dx.doi.org/10.5589/m02-092.

Frankenberg, C., Fisher, J.B., Worden, J., Badgley, G., et al., 2011. New global observations of the terrestrial carbon cycle from GOSAT: Patterns of plant fluorescence with gross primary productivity. Geophys. Res. Lett. 38 (17), http://dx.doi.org/10.1029/2011GL048738.

Frankenberg, C., O'Dell, C., Berry, J, Guanter, L., et al., 2014. Prospects for chlorophyll fluorescence remote sensing from the orbiting carbon observatory-2. Remote Sens. Environ. 147, 1–12. http://dx.doi.org/10.1016/j.rse.2014.02.007.

Friedlingstein, P., et al., 2022. Global carbon budget 2022. Earth Syst. Sci. Data 14 (11), 4811–4900. http://dx.doi.org/10.5194/essd-14-4811-2022.

Garbulsky, M.F., Peñuelas, J., Papale, D., Filella, I., 2008. Remote estimation of carbon dioxide uptake by a Mediterranean forest. Global Change Biol. 14 (12), 2860–2867. http://dx.doi.org/10.1111/j.1365-2486.2008.01684.x.

Gomes, V.C.F., Queiroz, G.R., Ferreira, K.R., 2020. An overview of platforms for big earth observation data management and analysis. Remote Sens. 12 (8), http://dx.doi.org/10.3390/rs12081253.

Gorelick, N., Hancher, M., Dixon, M., Ilyushchenko, S., Thau, D., Moore, R., 2017. Google Earth Engine: Planetary-scale geospatial analysis for everyone. Remote Sens. Environ. 202, 18–27. http://dx.doi.org/10.1016/j.rse.2017.06.031, Big Remotely Sensed Data: tools, applications and experiences.

Gu, M.H., Cho, C., Chu, H.Y., Kang, n.w., Lee, j.g., 2021. Uncertainty propagation on a nonlinear measurement model based on Taylor expansion. Meas. Control 54, 002029402198974. http://dx.doi.org/10.1177/0020294021989740.

Gu, L., Han, J., Wood, J.D., Chang, C.Y.Y., Sun, Y., 2019. Sun-induced Chl fluorescence and its importance for biophysical modeling of photosynthesis based on light reactions. New Phytol. 223 (3), 1179–1191. http://dx.doi.org/10.1111/nph.15796.

Guan, K., Berry, J.A., Zhang, Y., Joiner, J., et al., 2016. Improving the monitoring of crop productivity using spaceborne solar-induced fluorescence. Global Change Biol. 22 (2), 716–726. http://dx.doi.org/10.1111/gcb.13136.

Guanter, L., Bacour, C., Schneider, A., Aben, I., et al., 2021. The TROPOSIF global sun-induced fluorescence dataset from the Sentinel-5P TROPOMI mission. Earth Syst. Sci. Data 13 (11), 5423–5440. http://dx.doi.org/10.5194/essd-13-5423-2021.

Han, J., Chang, C.Y.Y., Gu, L., Zhang, Y., et al., 2022. The physiological basis for estimating photosynthesis from Chla fluorescence. New Phytol. 234 (4), 1206–1219. http://dx.doi.org/10.1111/nph.18045.

Haxeltine, A., Prentice, I.C., 1996. A general model for the light-use efficiency of primary production. Funct. Ecol. 10 (5), 551–561.

He, P., Ma, X., Han, Z., Meng, X., Sun, Z., 2022. Uncertainties of gross primary productivity of Chinese grasslands based on multi-source estimation. Front. Environ. Sci. 10, http://dx.doi.org/10.3389/fenvs.2022.928351.

Hersbach, H., Bell, B., Berrisford, P., Hirahara, S., et al., 2020. The ERA5 global reanalysis. Q. J. R. Meteorol. Soc. 146 (730), 1999–2049.

Hu, J., Liu, X., Liu, L., Guan, L., 2018. Evaluating the performance of the SCOPE model in simulating canopy solar-induced chlorophyll fluorescence. Remote Sens. 10 (2), http://dx.doi.org/10.3390/rs10020250.

Johnson, I.R., Riha, S.J., Wilks, D.S., 1996. Modelling daily net canopy photosynthesis and its adaptation to irradiance and atmospheric CO2 concentration. Agricult. Syst. 50 (1), 1–35. http://dx.doi.org/10.1016/0308-521X(95)00010-3.

Joiner, J., Yoshida, Y., Zhang, Y., Duveiller, G., et al., 2018. Estimation of terrestrial global gross primary production (GPP) with satellite data-driven models and eddy covariance flux data. Remote Sens. 10 (9), http://dx.doi.org/10.3390/rs10091346.

Jonard, F., Cannière, S.D., Brüggemann, N., Gentine, P., et al., 2020. Value of sun-induced chlorophyll fluorescence for quantifying hydrological states and fluxes: Current status and challenges. Agricult. Forest Meteorol. 291, 108088. http://dx.doi.org/10.1016/j.agrformet.2020.108088.

Jung, M., Reichstein, M., Bondeau, A., 2009. Towards global empirical upscaling of FLUXNET eddy covariance observations: Validation of a model tree ensemble approach using a biosphere model. Biogeosciences 6 (10), 2001–2013. http://dx.doi.org/10.5194/bg-6-2001-2009.

Jung, M., Reichstein, M., Margolis, H.A., Cescatti, A., et al., 2011. Global patterns of land-atmosphere fluxes of carbon dioxide, latent heat, and sensible heat derived from eddy covariance, satellite, and meteorological observations. J. Geophys. Res. Biogeosci. 116 (G3), http://dx.doi.org/10.1029/2010JG001566.

Jung, M., Schwalm, C., Migliavacca, M., Walther, S., et al., 2020. Scaling carbon fluxes from eddy covariance sites to globe: synthesis and evaluation of the FLUXCOM approach. Biogeosciences 17 (5), 1343–1365. http://dx.doi.org/10.5194/bg-17-1343-2020.

Keenan, T., Williams, C., 2018. The terrestrial carbon sink. Ann. Rev. Environ. Resour. 43 (1), 219–243. http://dx.doi.org/10.1146/annurev-environ-102017-030204.

Kim, J., Ryu, Y., Dechant, B., Lee, H., Kim, H., Kornfeld, A., Berry, J., 2021. Solar-induced chlorophyll fluorescence is non-linearly related to canopy photosynthesis in a temperate evergreen needleleaf forest during the fall transition. Remote Sens. Environ. 112362. http://dx.doi.org/10.1016/j.rse.2021.112362.

Kottek, M., Grieser, J., Beck, C., Rudolf, B., Rubel, F., 2006. World map of the Köppen-Geiger climate classification updated. Meteorol. Z. 15 (3), 259–263. http://dx.doi.org/10.1127/0941-2948/2006/0130, Publisher: E. Schweizerbart'sche Verlagsbuchhandlung.

Kovács, D.D., Reyes-Muñoz, P., Salinero-Delgado, M., Mészáros, V.I., Berger, K., Verrelst, J., 2023. Cloud-free global maps of essential vegetation traits processed from the TOA sentinel-3 catalogue in google earth engine. Remote Sens. 15 (13), 3404. http://dx.doi.org/10.3390/rs15133404.

Krinner, G., Viovy, N., de Noblet-Ducoudré, N., Ogée, J., et al., 2005. A dynamic global vegetation model for studies of the coupled atmosphere-biosphere system. Glob. Biogeochem. Cycles 19 (GB1015), 1–44. http://dx.doi.org/10.1029/2003GB002199, Publisher: American Geophysical Union.

Lasslop, G., Reichstein, M., Papale, D., Richardson, A.D., et al., 2010. Separation of net ecosystem exchange into assimilation and respiration using a light response curve approach: critical issues and global evaluation. Global Change Biol. 16 (1), 187–208. http://dx.doi.org/10.1111/j.1365-2486.2009.02041.x.

Li, X., Xiao, J., 2019. A global, 0.05-degree product of solar-induced chlorophyll fluorescence derived from OCO-2, MODIS, and reanalysis data. Remote Sens. 11 (5), http://dx.doi.org/10.3390/rs11050517.

Li, X., Xiao, J., 2022. TROPOMI observations allow for robust exploration of the relationship between solar-induced chlorophyll fluorescence and terrestrial gross primary production. Remote Sens. Environ. 268, 112748. http://dx.doi.org/10.1016/j.rse.2021.112748.

Li, Y., Yin, Y., Zhang, W., 2023. Water footprint assessment of major crops in henan province and reduction suggestions. Water 15 (6), http://dx.doi.org/10.3390/w15061135.

Liao, Z., Zhou, B., Zhu, J., Jia, H., Fei, X., 2023. A critical review of methods, principles and progress for estimating the gross primary productivity of terrestrial ecosystems. Front. Environ. Sci. 11, http://dx.doi.org/10.3389/fenvs.2023.1093095.

Liu, J., Chen, J.M., Cihlar, J., Park, W.M., 1997. A process-based boreal ecosystem productivity simulator using remote sensing inputs. Remote Sens. Environ. 62 (2), 158–175. http://dx.doi.org/10.1016/S0034-4257(97)00089-8.

Magney, T.S., Barnes, M.L., Yang, X., 2020. On the covariation of chlorophyll fluorescence and photosynthesis across scales. Geophys. Res. Lett. 47 (23), e2020GL091098. http://dx.doi.org/10.1029/2020GL091098.

Martín Belda, D., Anthoni, P., Wårlind, D., Olin, S., et al., 2022. LPJ-GUESS/LSMv1.0: a next-generation land surface model with high ecological realism. Geosci. Model Dev. 15 (17), 6709–6745. http://dx.doi.org/10.5194/gmd-15-6709-2022.

Mohammed, G.H., Colombo, R., Middleton, E.M., Rascher, U., et al., 2019. Remote sensing of solar-induced chlorophyll fluorescence (SIF) in vegetation: 50 years of progress. Remote Sens. Environ. 231, 111177. http://dx.doi.org/10.1016/j.rse.2019.04.030.

Monteith, J.L., 1972. Solar radiation and productivity in tropical ecosystems. J. Appl. Ecol. 9 (3), 747–766. http://dx.doi.org/10.2307/2401901.

Munro, R., Lang, R., Klaes, D., Poli, G., et al., 2016. The GOME-2 instrument on the metop series of satellites: instrument design, calibration, and level 1 data processing – an overview. Atmos. Meas. Tech. 9 (3), 1279–1301. http://dx.doi.org/10.5194/amt-9-1279-2016.

Papagiannopoulou, C., Miralles, D.G., Decubber, S., Demuzere, M., et al., 2017. A non-linear granger-causality framework to investigate climate–vegetation dynamics. Geosci. Model Dev. 10 (5), 1945–1960. http://dx.doi.org/10.5194/gmd-10-1945-2017.

Paris, J.-D., Ciais, P., Rivier, L., Chevallier, F., et al., 2012. Integrated carbon observation system. p. 12397.

Parker, G.G., 2020. Tamm review: Leaf Area Index (LAI) is both a determinant and a consequence of important processes in vegetation canopies. Forest Ecol. Manag. 477, 118496. http://dx.doi.org/10.1016/j.foreco.2020.118496.

Pastorello, G., et al., 2020. The FLUXNET2015 dataset and the ONEFlux processing pipeline for eddy covariance data. Sci. Data 7 (1), 225. http://dx.doi.org/10.1038/s41597-020-0534-3.

Pei, Y., Dong, J., Zhang, Y., Yuan, W., et al., 2022. Evolution of light use efficiency models: Improvement, uncertainties, and implications. Agricult. Forest Meteorol. 317, 108905. http://dx.doi.org/10.1016/j.agrformet.2022.108905.

Pierrat, Z., Magney, T., Parazoo, N.C., Grossmann, K., et al., 2022. Diurnal and seasonal dynamics of solar-induced chlorophyll fluorescence, vegetation indices, and gross primary productivity in the boreal forest. J. Geophys. Res. Biogeosciences 127 (2), e2021JG006588. http://dx.doi.org/10.1029/2021JG006588.

Pipia, L., Amin, E., Belda, S., Salinero-Delgado, M., Verrelst, J., 2021. Green LAI mapping and cloud gap-filling using Gaussian process regression in google earth engine. Remote Sens. 13 (3), http://dx.doi.org/10.3390/rs13030403.

Porcar-Castell, A., Malenovskỳ, Z., Magney, T., Van Wittenberghe, S., Fernández-Marín, B., et al., 2021. Chlorophyll a fluorescence illuminates a path connecting plant molecular biology to Earth-system science. Nature Plants 7 (8), 998–1009. http://dx.doi.org/10.1038/s41477-021-00980-4.

Porcar-Castell, A., Tyystjärvi, E., Atherton, J., Van der Tol, C., et al., 2014. Linking chlorophyll a fluorescence to photosynthesis for remote sensing applications: mechanisms and challenges. J. Exp. Bot. 65 (15), 4065–4095. http://dx.doi.org/10.1093/jxb/eru191.

Prentice, I.C., Cowling, S.A., 2013. Dynamic global vegetation models. In: Levin, S.A. (Ed.), Encyclopedia of Biodiversity (Second Edition), second ed. Academic Press, Waltham, pp. 670–689. http://dx.doi.org/10.1016/B978-0-12-384719-5.00412-3.

Prikaziuk, E., Migliavacca, M., Su, Z.B., Tol, C.v.d., 2023. Simulation of ecosystem fluxes with the SCOPE model: Sensitivity to parametrization and evaluation with flux tower observations. Remote Sens. Environ. 284, 113324. http://dx.doi.org/10.1016/j.rse.2022.113324.

Rasmussen, C.E., Williams, C.K.I., 2006. Gaussian Processes for Machine Learning. The MIT Press, New York.

Reich, P.B., 2012. Key canopy traits drive forest productivity. Proc. R. Soc. [Biol.] 279 (1736), 2128–2134. http://dx.doi.org/10.1098/rspb.2011.2270.

Reichstein, M., Ciais, P., Papale, D., Valentini, R., et al., 2007. Reduction of ecosystem productivity and respiration during the European summer 2003 climate anomaly: A joint flux tower, remote sensing and modelling analysis. Global Change Biol. 13 (3), 634–651. http://dx.doi.org/10.1111/j.1365-2486.2006.01224.x.

Reyes-Muñoz, P., Pipia, L., Salinero-Delgado, M., Belda, S., et al., 2022. Quantifying fundamental vegetation traits over europe using the sentinel-3 OLCI catalogue in google earth engine. Remote Sens. 14 (6), http://dx.doi.org/10.3390/rs14061347.

Rivera-Caicedo, J.P., Verrelst, J., Muñoz-Marí, J., Moreno, J., Camps-Valls, G., 2014. Toward a semiautomatic machine learning retrieval of biophysical parameters. IEEE J. Sel. Top. Appl. Earth Obs. Remote Sens. 7 (4), 1249–1259. http://dx.doi.org/10.1109/JSTARS.2014.2298752.

Robinson, N.P., Allred, B.W., Smith, W.K., Jones, M.O., et al., 2018. Terrestrial primary production for the conterminous United States derived from landsat 30 m and MODIS 250 m. Remote Sens. Ecol. Conserv. 4 (3), 264–280. http://dx.doi.org/10.1002/rse2.74.

Roy, S., 2023. Geeup: Simple CLI for earth engine uploads. http://dx.doi.org/10.5281/zenodo.7831458.

Ruimy, A., Saugier, B., Dedieu, G., 1994. Methodology for the estimation of terrestrial net primary production from remotely sensed data. J. Geophys. Res. 99, 5263–5284. http://dx.doi.org/10.1029/93JD03221.

Running, S., Mu, Q., Zhao, M., 2015. MOD17A2H MODIS/Terra Gross Primary Productivity 8-Day L4 Global 500 m SIN Grid V006. NASA EOSDIS Land Processes DAAC.

Ryu, Y., Baldocchi, D.D., Kobayashi, H., van Ingen, C., Li, J., et al., 2011. Integration of MODIS land and atmosphere products with a coupled-process model to estimate gross primary productivity and evapotranspiration from 1 km to global scales. Glob. Biogeochem. Cycles 25 (4), http://dx.doi.org/10.1029/2011GB004053.

Salinero-Delgado, M., Estévez, J., Pipia, L., Belda, S., et al., 2022. Monitoring cropland phenology on google earth engine using Gaussian process regression. Remote Sens. 14 (1), http://dx.doi.org/10.3390/rs14010146.

Saltelli, A., 2004. Global sensitivity analysis: An introduction. In: Proceedings of the 4th International Conference on Sensitivity Analysis of Model Output. SAMO 2004.

Schlau-Cohen, G.S., Berry, J., 2015. Photosynthetic fluorescence, from molecule to planet. Phys. Today 68 (9), 66–67. http://dx.doi.org/10.1063/PT.3.2924.

Scurlock, J., Johnson, K., Olson, R., 2003. NPP grassland: NPP estimates from biomass dynamics for 31 sites, 1948–1994, R1. http://dx.doi.org/10.3334/ORNLDAAC/654.

Seaton, G.G.R., Walker, D.A., 1990. Chlorophyll fluorescence as a measure of photosynthetic carbon assimilation. Proc. R. Soc. B 242 (1303), 29–35. http://dx.doi.org/10.1098/rspb.1990.0099.

Sharkey, T.D., 1985. Photosynthesis in intact leaves of C3 plants: Physics, physiology and rate limitations. Bot. Rev. 51 (1), 53–105. http://dx.doi.org/10.1007/BF02861058.

Siddiqi, A., Baber, S., de Weck, O., Durell, C., 2020. Error and uncertainty in Earth observation value chains. pp. 3158–3161. http://dx.doi.org/10.1109/IGARSS39084.2020.9323463.

Still, C.J., Berry, J.A., Collatz, G.J., DeFries, R.S., 2003. Global distribution of C3 and C4 vegetation: Carbon cycle implications. Glob. Biogeochem. Cycles 17 (1), 6–1–6–14. http://dx.doi.org/10.1029/2001GB001807.

Sun, Y., Frankenberg, C., Jung, M., Joiner, J., et al., 2018. Overview of Solar-Induced chlorophyll Fluorescence (SIF) from the Orbiting Carbon Observatory-2: Retrieval, cross-mission comparison, and global monitoring for GPP. Remote Sens. Environ. 209, 808–823. http://dx.doi.org/10.1016/j.rse.2018.02.016.

Sun, Y., Frankenberg, C., Wood, J., Schimel, D., et al., 2017. OCO-2 advances photosynthesis observation from space via solar-induced chlorophyll fluorescence. Science 358 (6360), http://dx.doi.org/10.1126/science.aam5747.

Tang, Y., Wang, Q., Tong, X., Atkinson, P.M., 2021. Integrating spatio-temporal-spectral information for downscaling Sentinel-3 OLCI images. ISPRS J. Photogramm. Remote Sens. 180, 130–150. http://dx.doi.org/10.1016/j.isprsjprs.2021.08.012.

Tol, C., Verhoef, W., Rosema, A., 2009a. A model for chlorophyll fluorescence and photosynthesis at leaf scale. Agricult. Forest Meteorol. 149, 96–105. http://dx.doi.org/10.1016/j.agrformet.2008.07.007.

Tol, C., Verhoef, W., Timmermans, J., Verhoef, A., Su, B., 2009b. An integrated model of soil-canopy spectral radiance observations, photosynthesis, fluorescence, temperature and energy balance. Biogeosciences Discuss. 6, http://dx.doi.org/10.5194/bgd-6-6025-2009.

Tramontana, G., Jung, M., Schwalm, C.R., Ichii, K., et al., 2016. Predicting carbon dioxide and energy fluxes across global FLUXNET sites with regression algorithms. Biogeosciences 13 (14), 4291–4313. http://dx.doi.org/10.5194/bg-13-4291-2016.

Tramontana, G., Migliavacca, M., Jung, M., Reichstein, M., et al., 2020. Partitioning net carbon dioxide fluxes into photosynthesis and respiration using neural networks. Global Change Biol. 26 (9), 5235–5253. http://dx.doi.org/10.1111/gcb.15203.

Van Wittenberghe, S., Sabater, N., Cendrero-Mateo, M., Tenjo, C., et al., 2021. Towards the quantitative and physically-based interpretation of solar-induced vegetation fluorescence retrieved from global imaging. Photosynthetica 59 (SPECIAL ISSUE), 438–457. http://dx.doi.org/10.32615/ps.2021.034.

Veefkind, P., Aben, I., McMullan, K., Förster, H., et al., 2012. TROPOMI on the ESA sentinel-5 precursor: A GMES mission for global observations of the atmospheric composition for climate, air quality and ozone layer applications. Remote Sens. Environ. 120, 70–83. http://dx.doi.org/10.1016/j.rse.2011.09.027.

Vermote, E., Tanre, D., Deuze, J., Herman, M., Morcette, J.-J., 1997. Second simulation of the satellite signal in the solar spectrum, 6S: an overview. IEEE Trans. Geosci. Remote Sens. 35 (3), 675–686. http://dx.doi.org/10.1109/36.581987.

Verrelst, J., Alonso, L., Camps-Valls, G., Delegido, J., Moreno, J., 2012a. Retrieval of vegetation biophysical parameters using Gaussian process techniques. IEEE Trans. Geosci. Remote Sens. 50 (5), 1832–1843. http://dx.doi.org/10.1109/TGRS.2011.2168962.

Verrelst, J., Dethier, S., Rivera, J.P., Munoz-Mari, J., Camps-Valls, G., Moreno, J., 2016a. Active learning methods for efficient hybrid biophysical variable retrieval. IEEE Geosci. Remote Sens. Lett. 13 (7), 1012–1016. http://dx.doi.org/10.1109/LGRS.2016.2560799.

Verrelst, J., Malenovský, Z., Tol, C., Camps-Valls, G., et al., 2019. Quantifying vegetation biophysical variables from imaging spectroscopy data: A review on retrieval methods. Surv. Geophys. 40, http://dx.doi.org/10.1007/s10712-018-9478-y.

Verrelst, J., Muñoz, J., Alonso, L., Delegido, J., et al., 2012b. Machine learning regression algorithms for biophysical parameter retrieval: Opportunities for sentinel-2 and-3. Remote Sens. Environ. 118, 127–139. http://dx.doi.org/10.1016/j.jag.2016.07.016.

Verrelst, J., Rivera, J.P., Gitelson, A., Delegido, J., Moreno, J., Camps-Valls, G., 2016b. Spectral band selection for vegetation properties retrieval using Gaussian processes regression. Int. J. Appl. Earth Obs. Geoinf. 52, 554–567. http://dx.doi.org/10.1016/j.jag.2016.07.016.

Verrelst, J., Romijn, E., Kooistra, L., 2012c. Mapping vegetation density in a heterogeneous river floodplain ecosystem using pointable CHRIS/PROBA data. Remote Sens. 4 (9), 2866–2889. http://dx.doi.org/10.3390/rs4092866.

Verrelst, J., van der Tol, C., Magnani, F., Sabater, N., et al., 2016c. Evaluating the predictive power of sun-induced chlorophyll fluorescence to estimate net photosynthesis of vegetation canopies: A SCOPE modeling study. Remote Sens. Environ. 176, 139–151. http://dx.doi.org/10.1016/j.rse.2016.01.018.

Vicent, J., Sabater Medina, N., Tenjo, C., Acarreta, J., et al., 2016. FLEX end-to-end mission performance simulator. IEEE Trans. Geosci. Remote Sens. 54, 1–9. http://dx.doi.org/10.1109/TGRS.2016.2538300.

Wang, Z., Li, Y., Su, X., Tao, S., Feng, X., et al., 2019. Patterns and ecological determinants of woody plant height in eastern eurasia and its relation to primary productivity. J. Plant Ecol. 12, http://dx.doi.org/10.1093/jpe/rtz025.

Wang, J., Sun, R., Zhang, H., Xiao, Z., Zhu, A., Wang, M., Yu, T., Xiang, K., 2021a. New global MuSyQ GPP/NPP remote sensing products from 1981 to 2018. IEEE J. Sel. Top. Appl. Earth Obs. Remote Sens. 14, 5596–5612. http://dx.doi.org/10.1109/JSTARS.2021.3076075.

Wang, S., Zhang, Y., Ju, W., Qiu, B., Zhang, Z., 2021b. Tracking the seasonal and inter-annual variations of global gross primary production during last four decades using satellite near-infrared reflectance data. Sci. Total Environ. 755, 142569. http://dx.doi.org/10.1016/j.scitotenv.2020.142569.

Whittaker, E.T., 1922. On a new method of graduation. Proc. Edinburgh Math. Soc. 41, 63–75. http://dx.doi.org/10.1017/S0013091500077853.

Wild, B., Teubner, I., Moesinger, L., Zotta, R.M., et al., 2022. VODCA2GPP – a new, global, long-term (1988–2020) gross primary production dataset from microwave remote sensing. Earth Syst. Sci. Data 14 (3), 1063–1085. http://dx.doi.org/10.5194/essd-14-1063-2022.

Williams, M., Rastetter, E.B., Fernandes, D.N., Goulden, M.L., Shaver, G.R., Johnson, L.C., 1997. Predicting gross primary productivity in terrestrial ecosystems. Ecol. Appl. 7 (3), 882–894. http://dx.doi.org/10.1890/1051-0761(1997)007[0882:PGPPIT]2.0.CO;2.

Wohlfahrt, G., Gerdel, K., Migliavacca, M., Rotenberg, E., et al., 2018. Sun-induced fluorescence and gross primary productivity during a heat wave. Sci. Rep. 8 (14169), 1–9. http://dx.doi.org/10.1038/s41598-018-32602-z.

Wolanin, A., Camps-Valls, G., Gómez-Chova, L., Mateo-García, G., et al., 2019. Estimating crop primary productivity with sentinel-2 and landsat 8 using machine learning methods trained with radiative transfer simulations. Remote Sens. Environ. 225, 441–457. http://dx.doi.org/10.1016/j.rse.2019.03.002.

Wong, C.Y., D'Odorico, P., Arain, M.A., Ensminger, I., 2020. Tracking the phenology of photosynthesis using carotenoid-sensitive and near-infrared reflectance vegetation indices in a temperate evergreen and mixed deciduous forest. New Phytol. 226 (6), 1682–1695. http://dx.doi.org/10.1111/nph.16479.

Xiao, J., Fisher, J.B., Hashimoto, H., Ichii, K., Parazoo, N.C., 2021. Emerging satellite observations for diurnal cycling of ecosystem processes. Nature Plants 7 (7), 877–887. http://dx.doi.org/10.1038/s41477-021-00952-8.

Xie, X., Li, A., Chen, J., Guan, X., Leng, J., 2022. Quantifying scaling effect on gross primary productivity estimation in the upscaling process of surface heterogeneity. J. Geophys. Res. Biogeosciences 127, http://dx.doi.org/10.1029/2021JG006775.

Xie, X., Li, A., Jin, H., Tan, J., et al., 2019. Assessment of five satellite-derived LAI datasets for GPP estimations through ecosystem models. Sci. Total Environ. 690, 1120–1130. http://dx.doi.org/10.1016/j.scitotenv.2019.06.516.

Yang, S., Yang, J., Shi, S., Song, S., et al., 2022. An exploration of solar-induced chlorophyll fluorescence (SIF) factors simulated by SCOPE for capturing GPP across vegetation types. Ecol. Model. 472, 110079. http://dx.doi.org/10.1016/j.ecolmodel.2022.110079.

Yao, L., Liu, Y., Yang, D., Cai, Z., et al., 2022. Retrieval of solar-induced chlorophyll fluorescence (SIF) from satellite measurements: comparison of SIF between TanSat and OCO-2. Atmos. Meas. Tech. 15 (7), 2125–2137. http://dx.doi.org/10.5194/amt-15-2125-2022.

Zeng, J., Matsunaga, T., Tan, Z.H., Saigusa, N., et al., 2020. Global terrestrial carbon fluxes of 1999–2019 estimated by upscaling eddy covariance data with a random forest. Sci. data 7, 313. http://dx.doi.org/10.1038/s41597-020-00653-5.

Zhang, Y., Song, C., Sun, G., Band, L.E., et al., 2016. Development of a coupled carbon and water model for estimating global gross primary productivity and evapotranspiration based on eddy flux and remote sensing data. Agricult. Forest Meteorol. 223, 116–131. http://dx.doi.org/10.1016/j.agrformet.2016.04.003.

Zhang, Y., Xiao, X., Wu, X., Zhou, S., et al., 2017. A global moderate resolution dataset of gross primary production of vegetation for 2000–2016. Sci. Data 4 (1), 1–13. http://dx.doi.org/10.1038/sdata.2017.165.

Zhang, Y., Ye, A., 2022. Uncertainty analysis of multiple terrestrial gross primary productivity products. Global Ecol. Biogeogr. 31 (11), 2204–2218. http://dx.doi.org/10.1111/geb.13578.

Zhao, F., Ma, W., Köhler, P., Ma, X., et al., 2022. Retrieval of red solar-induced chlorophyll fluorescence with TROPOMI on the sentinel-5 precursor mission. IEEE Trans. Geosci. Remote Sens. 60, 1–14. http://dx.doi.org/10.1109/TGRS.2022.3162726.